

# 1 Unusual *Hemiaulus* Bloom Influences Ocean Productivity in 2 Northeast U.S. Shelf Waters

3 S. Alejandra Castillo Cieza<sup>1</sup>, Rachel H.R. Stanley<sup>1\*</sup>, Pierre Marrec<sup>2</sup>, Diana N. Fontaine<sup>2</sup>, E.  
4 Taylor Crockford<sup>3</sup>, Dennis J. McGillicuddy Jr.<sup>3</sup>, Arshia Mehta<sup>1</sup>, Susanne Menden-Deuer<sup>2</sup>, Emily  
5 E. Peacock<sup>3</sup>, Tatiana A. Rynearson<sup>2</sup>, Zoe O. Sandwith<sup>3,4</sup>, Weifeng (Gordon) Zhang<sup>3</sup>, and Heidi  
6 M. Sosik<sup>3</sup>

7 <sup>1</sup>Chemistry Department, Wellesley College, Wellesley, 02481, USA

8 <sup>2</sup>Graduate School of Oceanography, University of Rhode Island, Narragansett, 02882, USA

9 <sup>3</sup>Woods Hole Oceanographic Institution, Woods Hole, MA, 02543, USA

10 <sup>4</sup>Now at the Hakai Institute, Pruth Harbour, Calvert Island, BC, Canada

11 \*Correspondence to: Rachel H. R. Stanley (rachel.stanley@wellesley.edu)

12 **Abstract.** Ocean production and trophic transfer rates, including Net Community Production (NCP), Net Primary  
13 Production (NPP), Gross Oxygen Production (GOP), and microzooplankton grazing rates are key metrics for  
14 understanding marine ecosystem dynamics and impacts on biogeochemical cycles. Because of its temperate location  
15 and high dynamic range of environmental conditions, and long-term extensive human utilization activity, the long-  
16 term ecological research site in the coastal Northeastern U.S. Shelf (NES) of the Northwestern Atlantic Ocean offers  
17 an ideal opportunity to understand how productivity shifts in response to changes in planktonic community  
18 composition. While Ocean production and trophic transfer rates, including Net Community Production (NCP), Net  
19 Primary Production (NPP), Gross Oxygen Production (GOP), and microzooplankton grazing rates are key metrics  
20 for understanding marine ecosystem dynamics and associated impacts on biogeochemical cycles. Although small  
21 phytoplankton usually dominate phytoplankton community composition and Chl-a concentration in the NES waters  
22 during the summer, in August 2019, a bloom of the large diatom genus *Hemiaulus*, with N<sub>2</sub> fixing symbionts, was  
23 observed in the mid-shelf region during the summer of 2019; NCP was 2.5 to 9 times higher when *Hemiaulus*  
24 dominated phytoplankton carbon compared to NCP throughout the same geographic area during the summers of  
25 2020–2022. The *Hemiaulus* bloom in summer 2019 also coincided with higher trophic transfer efficiency from  
26 phytoplankton to microzooplankton, higher GOP and NPP, and higher sea surface temperatures than in the summers  
27 2020–2022. This study shows suggests that the presence dominance of an atypical phytoplankton community that  
28 alters the typical size distribution of the primary producers can greatly significantly influence productivity and  
29 trophic transfer, highlighting the dynamic nature of the coastal ocean. Notably, summer 2018 NCP levels were also  
30 high although the size distribution of Chl-a was typical and an atypical phytoplankton community was present or  
31 observed. A better understanding of the dynamics of the NES in terms of biological productivity is of primary  
32 importance, especially in the context of changing environmental conditions due to climate processes.

## 33 1 Introduction

34 Oceans regulate atmospheric carbon dioxide (CO<sub>2</sub>) concentrations and support life on Earth via several mechanisms  
35 (Friedlingstein et al., 2022). One of these mechanisms is the biological pump, which involves biological, physical,  
36 and chemical processes that aid in transporting and sequestering organic carbon from CO<sub>2</sub> (Boyd et al., 2019). As  
37 the main primary producers in the ocean, phytoplankton play a major role in the biological pump (Field et al., 1998).  
38 Diatoms, a type of photosynthetic algae, are believed to account for nearly half of net marine primary productivity  
39 globally and are important contributors to the biological pump (Jin et al., 2006). Diatoms characteristically thrive in  
40 nutrient-rich surface layers and turbulent conditions, and are thus typically found at high latitudes and in coastal  
41 upwelling regions (Armbrust, 2009). However, new technology (e.g., molecular biology and imaging) has revealed  
42 that diatoms may be more prevalent in low nutrient, oligotrophic systems than traditionally considered (Malviya et  
43 al., 2016), likely due to unique metabolic capabilities involving nutrient acquisition strategies that enable their  
44 survival in low nutrient regimes. (Marcellet, 1978).

45 One specific metabolic capability within diatoms is the ability to form a symbiosis with nitrogen-fixing  
46 cyanobacteria. This symbiosis, known as a diatom-diazotroph association, has been observed around the globe,  
47 mostly in oligotrophic regions (Foster and Zehr, 2019), but also in temperate continental shelf waters (Wang et al.,  
48 2021). Furthermore, some diatom-diazotroph association have the capability to grow very quickly, forming  
49 localized blooms (Villareal et al., 2011). Diatom-diazotroph blooms, specifically involving the diatom genus  
50 *Hemiaulus* and the symbiont *Richelia*, have been found in warm, stratified waters in various regions around the  
51 globe and have been associated with high carbon export observed via a combination of modern oceanographic  
52 measurements and paleo-flux case studies (Kemp and Villareal, 2013; Malviya et al., 2016). Examples include  
53 blooms in the eastern Equatorial Atlantic (Foster and Zehr, 2006), tropical North Atlantic (Carpenter et al., 1999;  
54 Subramaniam et al., 2008), North Pacific Subtropical Gyre (Dore et al., 2008; Villareal et al., 2011), and South  
55 China Sea (Grosse et al., 2010). Furthermore, at the ALOHA site in the Pacific Ocean north of Hawaii, blooms of  
56 the *Hemiaulus-Richelia* association can last as long as 30 days and contribute significantly (20%) to annual carbon  
57 flux in this region (Karl et al., 2012; Kemp and Villareal, 2018; Karl et al., 2012). As described by these examples,  
58 diatoms, Diatoms with nitrogen-fixing symbionts are thus important contributors to primary productivity and carbon  
59 export, especially at times when surface waters are depleted of dissolved inorganic nitrogen (Pyle et al., 2020; Tang  
60 et al., 2020; Tang et al., 2020).

61 An intense bloom of *Hemiaulus* and its symbiont *Richelia* was observed in summer 2019 in temperate  
62 Northeast U.S. Shelf (NES) surface waters. The NES region in the Northwestern Atlantic Ocean is particularly  
63 productive, favoring enhanced inorganic carbon sequestration by the biological pump, and supports an ecologically  
64 and economically important ecosystem (Townsend et al., 2006). Like other marine regions, the NES ecosystem food  
65 web is fueled by phytoplankton which are the main primary producers and, which play a fundamental components  
66 role in the ecosystem function (e.g. Mouw and Yoder, 2005; O'Reilly, O'Reilly, and Zetlin, 1998; Yoder et al.,  
67 2002). Productivity is heavily influenced by abiotic factors in the NES region. For instance, strong seasonal  
68 variations in water temperature, stratification and cross-shelf advection on the NES affect nutrient supply and lead to  
69 seasonal shifts in phytoplankton productivity and species composition (Li et al., 2015; Oliver et al., 2022; Zhang et  
70 al., 2023). Furthermore, the water temperature of the NES is rising faster than the global average (Chen et al., 2020;  
71 Karmalkar and Horton, 2021; Shearman and Lentz, 2010), leading to unknown consequences for phytoplankton  
72 community composition and productivity within this important and dynamic coastal region.

73 To further understand phytoplankton population dynamics and their influence on the ocean's biological  
74 pump, the NES Long-Term Ecological Research (NES-LTER, <https://nes-lter.whoi.edu/>) project investigates  
75 primary productivity, food web structure and ecosystem dynamics with a focus on southern New England coastal  
76 waters. As part of the NES-LTER project, phytoplankton and zooplankton community composition, phytoplankton  
77 growth rates, microzooplankton grazing rates, and productivity rates are determined on week-long research cruises  
78 which have occurred quarter-annually since 2018. To quantify productivity, several different rates are estimated  
79 from data collected on these cruises, including Gross Oxygen Production (GOP), Net Primary Production (NPP),  
80 Net Community Production (NCP) and export efficiency ratios (NCP/GOP). GOP is similar to Gross Primary  
81 Production; it represents total photosynthesis in oxygen units and also includes photoprocesses that produce oxygen  
82 (Juraneck and Quay, 2013). NPP is photosynthetic production minus autotrophic respiration and thus represents the  
83 net production activity of the phytoplankton community. NCP is the balance of photosynthesis and community  
84 respiration (autotrophic plus heterotrophic) and is equal, on long enough spatial and temporal scales, to the amount  
85 of carbon exported out of the surface of the ocean (Emerson, 2014). The NCP/GOP ratio, analogous to the f-ratio  
86 (Dugdale and Goering, 1967), is indicative of export efficiency, with a high ratio implying that the community is  
87 exporting most of the carbon (organic matter) produced and thus recycling only a little (Juraneck and Quay, 2013).

88 The composition and size structure of the phytoplankton community in the NES-LTER study are  
89 investigated concurrently from automated imaging and size-fractionated chlorophyll-a (Chl-a). In winter, the NES  
90 waters tend to be nutrient-rich due to enhanced vertical mixing and input of river and estuary waters that promote  
91 high levels of surface Chl-a, with a dominance of large phytoplankton cells ( $>10\ \mu\text{m}$ ) that are growing slowly  
92 (Marrec et al., 2021). Conversely, during a typical summer, nutrients become depleted in the surface mixed layer,  
93 leading to low Chl-a concentrations dominated by fast-growing small phytoplankton cells ( $<10\ \mu\text{m}$ ) (Marrec et al.,  
94 2021; O'Reilly and Zetlin, 1998; Marrec et al., 2021; O'Reilly and Zetlin, 1998).

95 To complement production estimates and phytoplankton community structure observations, the flow of  
96 carbon from primary producers to higher trophic levels on the NES has also been investigated. Microzooplankton,  
97 protists smaller than  $200\ \mu\text{m}$ , are a crucial link between primary producers and higher trophic levels because they  
98 often consume 60–70% of daily primary production (Landry and Calbet, 2004; Schmoker et al., 2013). In the NES,  
99 while phytoplankton grow faster during the summer than in winter, microzooplankton grazing rates tend to stay  
100 relatively constant across seasons (Marrec et al., 2021). Thus, during winter, phytoplankton growth rates and

101 microzooplankton grazing rates are typically well coupled and show a close 1:1 ratio, with microzooplankton  
102 consuming most of the primary production (Marrec et al., 2021). During the summer, the phytoplankton growth and  
103 microzooplankton grazing rates are typically decoupled, with higher growth rates than in winter, but grazing rates in  
104 the same range, leading to less than 50% of the primary production consumed by microzooplankton. The degree of  
105 coupling between microzooplankton grazing and phytoplankton growth rates is associated with phytoplankton size  
106 structure (Marrec et al., 2021) and likely species composition, and is an important indicator of the trophic transfer  
107 efficiency from phytoplankton to microzooplankton, at the base of the planktonic food web.

108 Here, we examined the association between productivity, phytoplankton composition and  
109 microzooplankton grazing, key components of trophic transfer efficiency and thus ecosystem function. During a  
110 NES-LTER cruise in summer 2019, we observed an anomalous relationship between growth and grazing rates, as  
111 well as dramatically different productivity rates and community composition compared to other summer cruises in  
112 the NES region. We thus investigated how a diatom bloom of *Hemiaulus*, with diazotrophic symbionts, affected  
113 metrics of productivity and grazing on the NES during the summer of 2019. Our results provide insights into the  
114 effects of community composition on productivity rates.

## 115 2 Methods

116 Measurements of environmental conditions, chemical and biological stocks, and productivity and grazing rates were  
117 conducted on multiple cruises within the framework of the NES-LTER program (Table 1). Measurements from three  
118 other cruises from different projects on the NES were also included in this analysis for comparison (project names in  
119 Table 1) and *Hemiaulus* abundances were further compared to an additional 26 cruises in the NES (Table S1).  
120 From this time series, we were able to better understand an event that was observed on the 2019 NES-LTER  
121 summer cruise (EN644) which occurred from August 19 to 25 (Table 1). Some data during that event, such as  
122 surface seawater temperature (SST), salinity (SSS), NCP rates, and phytoplankton composition were collected  
123 continuously from the underway system (i.e., km-scale resolution every 0.1 to 6 km depending on the measurement  
124 type and ship speed), while other parameters (e.g., NPP, grazing rates, Chl-a, nutrients) were measured discretely at  
125 the NES-LTER stations (Fig. 1, Table S2). Main stations were located with ~ 19 km spacing on a north-to-south  
126 transect primarily along 70°53'70.883" W. Fig. 1 shows the cruise track for the August 2019 NES-LTER  
127 cruise, but all the other NES-LTER cruises had a near identical cruise track. In particular, the mid-shelf region,  
128 which is where the *Hemiaulus* bloom primarily occurred, corresponds to 50 – 100 m water depth and was bounded  
129 by latitudes 40.980°N to 40.327°N. The mid-shelf region contains four stations. Exact locations and dates of when  
130 the mid-shelf stations were occupied is provided in Table S2.

131 Fig. 1 and contains 4 stations. At each station, water was collected via Niskin bottles mounted on a CTD-  
132 rosette (conductivity-temperature-depth, Seabird SBE32 Carousel Water Sampler). The CTD-rosette system  
133 consisted of a 24-bottle rosette frame with 10-L Niskin bottles. Depth, temperature, and salinity were collected with  
134 a SBE911 CTD (Seabird Electronics) equipped with additional sensors for chlorophyll fluorescence (WET Labs  
135 ECO-AFL/FL), photosynthetically active radiation (PAR, Biospherical Instruments® QSP2000), and beam  
136 attenuation (WET Labs C-Star 25-cm transmissometer). The Niskin bottles were closed at various depths ranging  
137 from surface to near bottom, based on the depths of the mixed layer, euphotic zone, and Chl-a maximum. Mixed  
138 layer depths were calculated from the temperature and salinity data from the CTD with the threshold method where  
139 the mixed layer was taken to be the depth where the density difference between the surface and bottom of the mixed  
140 layer was greater than  $\Delta\sigma_t = 0.125 \text{ kg m}^{-3}$  (De Boyer Montégut et al., 2004). Mixed layer depths were confirmed to  
141 be similar when a gradient criterion with a difference of  $0.0125 \text{ kg m}^{-3}$  was used instead (Kara et al., 2000).  
142 Euphotic Zone was taken to be the depth at which light was 1% of the surface value. Chl-a max was chosen based  
143 on the depth with maximum fluorescence observed in the CTD cast. Water from the Niskins was used to quantify a  
144 number of parameters as described in Sections 2.2 through 2.5.

145 +

146 The underway system consisted of continuous surface seawater pumped throughout the ship by an impeller pump  
147 and a diaphragm pump located near the ship's bow. Using water from the impeller pump, continuous measurements  
148 of surface temperature and salinity were obtained from a Seabird SBE38 (temperature) sensor installed at the water  
149 intake, and by a Seabird SBE45 sensor (temperature and salinity) located further away in the underway system.  
150 Because the diaphragm pump is less likely to damage plankton (Cetinic et al., 2016), its underway flow was used for  
151 measurements to quantify NCP (Section 2.1), GOP (Section 2.2), and phytoplankton community composition  
152 (Section 2.8). The ship steamed both south and north along the longitude 70.883°W and thus over the 6-day cruise,

Formatted: Indent: First line: 0.5"

153 the underway data sampled the same locations at multiple points in time. Stations were only occupied at one time  
154 per cruise.

155

156

157

158 **Table 1.** Dates of the summer cruises, as well as project and ship names and cruise numbers, that are presented in  
159 this paper. Project name abbreviations are as follows: OTZ– Ocean Twilight Zone, SPIROPA–Shelfbreak  
160 Productivity Interdisciplinary Research Operation at the Pioneer Array (Oliver et al., 2021), and EcoMon–  
161 Ecosystem Monitoring program run by the National Oceanic and Atmospheric Administration. Cruise tracks for the  
162 NES-LTER transects are shown in Fig. 1. The SPIROPA and OTZ cruises followed the same longitude 70.883°W  
163 when in the mid-shelf region and thus data used from those cruises is collocated with the NES-LTER data.

Cruise Name	Start date/End date	Project name	Ship name
EN617	20 July 2018 – 25 July 2018	NES-LTER	<i>R/V Endeavor</i>
TN368	05 July 2019 – 18 July 2019	SPIROPA	<i>R/V Thomas G. Thompson</i>
HB1907	25 July 2019 – 08 Aug 2019	OTZ	<i>NOAA Ship Henry B Bigelow</i>
GU1902	16 Aug 2019 – 29 Aug 2019	EcoMon	<i>NOAA Ship Gordon Gunter</i>
EN644	20 Aug 2019 – 25 Aug 2019	NES-LTER	<i>R/V Endeavor</i>
EN655	25 July 2020 – 28 July 2020	NES-LTER	<i>R/V Endeavor</i>
EN668	16 July 2021 – 21 July 2021	NES-LTER	<i>R/V Endeavor</i>
EN687	29 July 2022 – 03 Aug 2022	NES-LTER	<i>R/V Endeavor</i>

Formatted Table

164 The underway system consisted of continuous surface seawater pumped throughout the ship by an impeller pump  
165 and a diaphragm pump located near the ship's bow. Using water from the impeller pump, continuous measurements  
166 of surface temperature and salinity were obtained from a Seabird SBE28 (temperature) sensor installed at the water  
167 intake and by a Seabird SBE 15 sensor (temperature and salinity) located further away in the underway system.

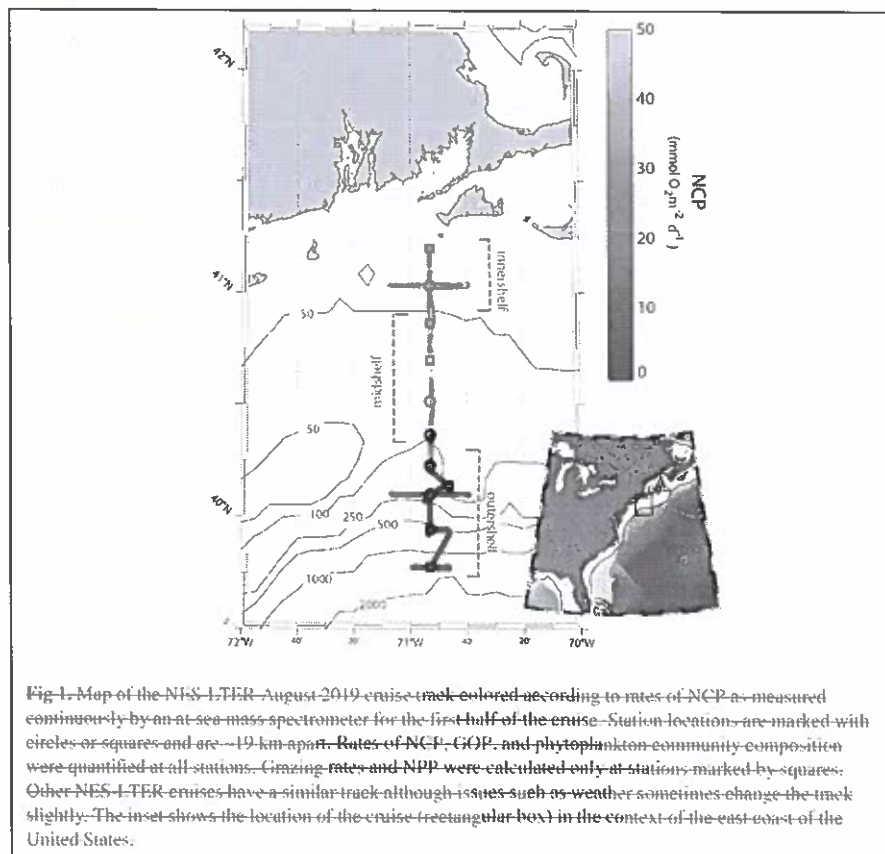


Fig. 1. Map of the NES LTER August 2019 cruise track colored according to rates of NCP as measured continuously by an at-sea mass spectrometer for the first half of the cruise. Station locations are marked with circles or squares and are ~19 km apart. Rates of NCP, GPP, and phytoplankton community composition were quantified at all stations. Grazing rates and NPP were calculated only at stations marked by squares. Other NES LTER cruises have a similar track although issues such as weather sometimes change the track slightly. The inset shows the location of the cruise (rectangular box) in the context of the east coast of the United States.

168 Because the diaphragm pump is less likely to damage plankton, its underway flow was used for measurements to  
 169 quantify NCP (Section 2.1), GPP (Section 2.2) and phytoplankton community composition (Section 2.6).

Formatted: Font: Not Bold

## 170 2.1 Net Community Production

171 Net community production rates were calculated from  $O_2/Ar$  ratios measured by an at-sea Equilibrator Inlet  
 172 Mass Spectrometer (EIMS) (Cassar et al., 2009) analyzing water from the ship's underway system and from discrete  
 173 samples collected from both CTD Niskin bottles and from the underway system. The EIMS was used to collect  
 174 continuous data on  $O_2/Ar$  ratios via the diaphragm pump of the underway system that, on the *R/V Endeavor*, pumps  
 175 seawater from a depth of 5 m. The underway system seawater flows through a debubbler into a bucket at a constant  
 176 rate that allows for continuous overflow for consistent head pressure. Water is then pumped from the bucket at ~1.1  
 177  $L\ min^{-1}$  by a gear pump through two filters: a bag with a 25- $\mu m$  pore size, and a 2-layered sock with a 5- $\mu m$  inner  
 178 and 100- $\mu m$  outer pore size. The gear pump then pushes the water through an equilibrator membrane contactor  
 179 cartridge (Liqui-Cel Extra-Flow 2.5x8 model G540). The equilibrated headspace gas from the cartridge is then dried  
 180 by flowing through the dessicants Nafion and Drierite and then passed via a fused silica capillary into a Hiden  
 181 Residual Gas Analyzer (RGA) (HAL 7) quadrupole mass spectrometer. Details of the equilibration method can be  
 182 found in Manning et al. (2016), but in this instance were modified to not use SAES getters as they would have  
 183 removed the  $O_2$ . The EIMS was operated throughout the whole cruise (starting one hour after the ship left port and

Formatted: Indent: First line: 0.5"

184 ending a few hours before return to port). To calibrate the mass spectrometer, the capillary was switched to an air  
185 inlet for twenty minutes approximately every six hours as the ratio of O<sub>2</sub>/Ar in air is stable and well-known.  
186 Additionally, bottle samples were collected from the underway system at least once per day and were subsequently  
187 measured on an isotope ratio mass spectrometer at Woods Hole Oceanographic Institution (see Section 2.2). These  
188 bottle samples were used to provide additional calibration as necessary—such additional corrections changed the  
189 O<sub>2</sub>/Ar ratios by at most 0.67%.

190 The O<sub>2</sub>/Ar ratios were then used to calculate NCP (Hendricks et al., 2004; Juranek and Quay, 2005;  
191 Stanley et al., 2010). With data from the EIMS and the bottle samples, the biological oxygen saturation Δ(O<sub>2</sub>/Ar)  
192 was calculated via the equation below:

193 
$$\Delta \left( \frac{O_2}{Ar} \right) = \frac{\left( \frac{O_2}{Ar} \right)_{smp}}{\left( \frac{O_2}{Ar} \right)_{eq}} - 1 \quad (1)$$

194  
195

Formatted: Font color: Black

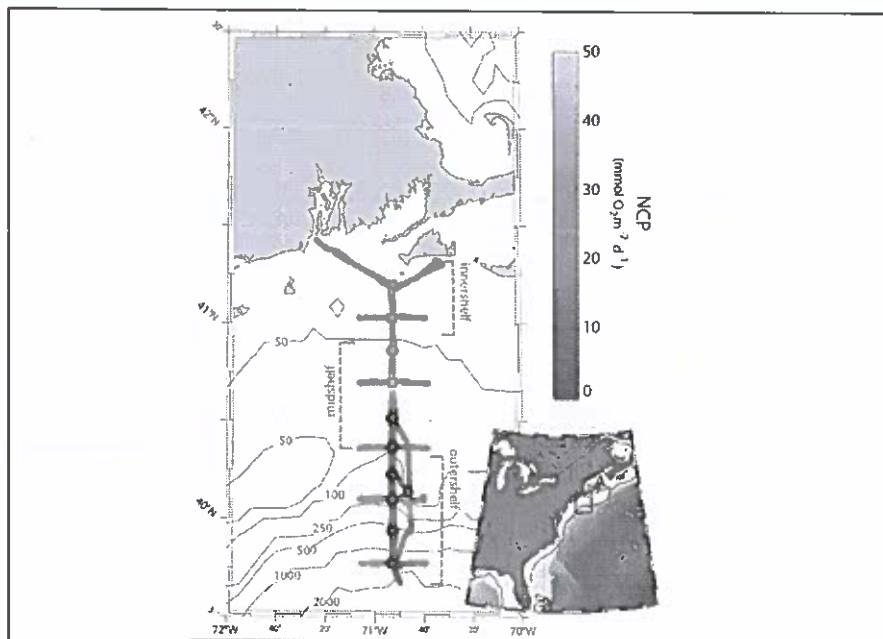


Fig 1. Map of the NES-LTER August 2019 cruise track colored according to rates of NCP as measured continuously by an at-sea mass spectrometer for the second half of the cruise. Station locations are marked with circles or squares and are ~19 km apart. Rates of NCP, GOP, and phytoplankton community composition were quantified at all stations. Grazing rates and NPP in 2019 to 2022 were calculated only at stations marked by squares. Other NES-LTER cruises have a similar track, although issues such as weather sometimes change the track slightly and in 2018. The inset shows the location of the cruise (rectangular box) in the context of the east coast of the United States.

196 where  $(O_2/Ar)_{mixt}$  represents the ratio of  $O_2$  to Ar ion currents detected by the EIMS after being calibrated with  
 197 bottle data, and  $(O_2/Ar)_{eq}$  represents the ratio of equilibrium concentrations of the gases determined from the gases'  
 198 solubility (Garcia and Gordon, 1992; Hamme and Emerson, 2004) (Garcia and Gordon, 1992; Hamme and Emerson,  
 199 2004) at the seawater temperature and salinity.

200 The NCP integrated over the mixed layer, in units of  $mmol O_2 m^{-2} d^{-1}$ , is calculated as

201  
 202 
$$NCP = \Delta \left( \frac{O_2}{Ar} \right) [O_2]_{eq} k \rho \quad (2)$$

203 where  $[O_2]_{eq}$  represents the equilibrium concentration of  $O_2$  at the relevant temperature and salinity ( $mmol kg^{-1}$ ).  $k$  is  
 204 the weighted gas transfer velocity ( $m d^{-1}$ ), and  $\rho$  is the density of seawater ( $kg m^{-3}$ ) (Millero and Poisson, 1981). The  
 205 weighted gas transfer velocity is a time-weighted average from over the past 30 days calculated as described in  
 206 Reuer et al. (2007), with the gas exchange parameterization of Stanley et al. (2009) and wind speeds from NCEP  
 207 Reanalysis (Kalnay et al., 1996; Kistler et al., 2001). Many physical considerations altering  $O_2$  saturations, such as  
 208 changes in temperature and bubble injection, do not need to be considered due to the inclusion of Ar which has  
 209 similar solubility and diffusivity as  $O_2$ ; however, a few assumptions were made for these calculations. Firstly, this  
 210 equation assumes steady state within the mixed layer, i.e. no change in  $O_2/Ar$  in the ocean with time. While  $O_2/Ar$   
 211 was likely changing in actuality, assuming steady state simply means that the rates calculated reflect an  
 212 exponentially weighted average of NCP over the past few residence times of oxygen (residence time equals a few



213 days in these conditions) (Teeter et al., 2018). Thus, the assumption of steady state does not majorly impact our  
 214 conclusions. We were not able to calculate the time rate of change term in O<sub>2</sub>/Ar (Manning et al., 2017b) because  
 215 the cruise was not Lagrangian, and even though the ship returned to the same geographic location, the water at that  
 216 location changed due to ocean currents. To check the assumption that there is negligible respiration within the ship's  
 217 lines (Juranek et al., 2010), bottle samples were collected in duplicate from Niskins at the same time as samples  
 218 were collected from the underway system several times during every cruise: gas concentrations in the bottle samples  
 219 from the underway and Niskin were identical within measurement errors, confirming there was no detectable  
 220 respiration in the ship's line.

## 221 2.2 Gross Oxygen Production

222 Discrete samples of triple oxygen isotopes (TOI) were collected from the surface Niskin bottles on the CTD-rosette  
 223 system at all stations as well as from the underway system between stations. Samples from the CTD-rosette system  
 224 were also collected from bottles fired at ~ 5 m below the mixed layer and often one greater depth to provide  
 225 information for assessing whether vertical corrections to O<sub>2</sub>/Ar ratios were significant. Samples were collected in  
 226 custom-made ~500-mL sample bottles which were pre-poisoned with 100 µl of saturated mercuric chloride solution  
 227 and filled with around 300 mL of seawater from the underway system or from the Niskin at each station (Stanley et  
 228 al., 2015). Samples were brought to Woods Hole Oceanographic Institution where they were analyzed for TOI with  
 229 a custom-made processing line and a ThermoFisher MAT 253 isotope ratio mass spectrometer as detailed in Stanley  
 230 et al (2015). The same samples were also analyzed for O<sub>2</sub>/Ar which yielded rates of NCP from discrete data as well  
 231 as an independent method for calibrating the EIMS (see above). Corrections for the effect of argon on the triple  
 232 oxygen isotope ratio and the effect of varying sizes of the sample vs. reference standard were made for every  
 233 sample. Reproducibility from duplicate samples collected on these cruises ranged from 4 to 8 per meg for <sup>17</sup>Δ, 0.008  
 234 to 0.03 per mil for δ<sup>17</sup>O, and 0.008 to 0.05 per mil for δ<sup>18</sup>O depending on the cruise.

235 From these samples, GOP is calculated in units of mmol O<sub>2</sub> m<sup>-2</sup> d<sup>-1</sup> following Prokopenko et al., (2011)  
 236 according to:

$$237 \text{ GOP} = k O_{\text{eq}} \frac{\frac{X_{\text{dis}}^{17} - X_{\text{eq}}^{17}}{X_{\text{dis}}^{16}} - \lambda \frac{X_{\text{dis}}^{18} - X_{\text{eq}}^{18}}{X_{\text{dis}}^{16}}}{\frac{X_{\text{dis}}^{17} - X_{\text{eq}}^{17}}{X_{\text{dis}}^{16}} - \lambda \frac{X_{\text{dis}}^{18} - X_{\text{eq}}^{18}}{X_{\text{dis}}^{16}}} \quad (3)$$

238 where  $k$  again represents the time-weighted gas transfer velocity (m d<sup>-1</sup>),  $O_{\text{eq}}$  represents the equilibrium  
 239 concentration of oxygen,  $\lambda$  represents the respiration slope factor = 0.5179,  $X_{\text{dis}}^*$  represents the ratio of isotopes  
 240 (<sup>\*</sup>O/<sup>16</sup>O) dissolved in the sample,  $X_{\text{eq}}^*$  represents the ratio of isotopes (<sup>\*</sup>O/<sup>16</sup>O) dissolved in seawater equilibrated  
 241 with the atmosphere, and  $X_{\text{P}}^*$  stands for the ratio of isotopes (<sup>\*</sup>O/<sup>16</sup>O) in oxygen that was produced via  
 242 photosynthesis. The photosynthetic end member used was the average of the phytoplankton value determined by  
 243 Barkan and Luz (2011) and the Vienna Standard Mean Ocean Water (VSMOW) was used for the isotopic composition  
 244 of oxygen in H<sub>2</sub>O. The actual isotopic composition of H<sub>2</sub>O was measured in a subset of samples to see if corrections  
 245 needed to be made (Manning et al., 2017a). It was found to be very similar to VSMOW, leading to an error of less  
 246 than 10% in GOP due to isotopic water variations.

247 Confirmation that the water from the underway system was representative of the oceanic TOI signature of  
 248 dissolved oxygen was obtained by comparing samples collected from the underway system to those collected  
 249 concurrently from the surface Niskin bottle. All cruises, other than 2019, showed that there was statistically no  
 250 difference in TOI between water from the underway system and the CTD and thus that the water from the underway  
 251 system was representative of the mixed layer at that location and time. During the summer of 2019, the water from  
 252 the underway system had TOI values 4.1 per meg lower than that from the CTD – this is within measurement errors  
 253 but since it might have led to systematic biases, we corrected for this offset before calculating GOP from the data.  
 254 The GOP rates, along with the NCP rates, represent productivity integrated throughout the mixed layer.

## 255 2.3 Net Primary Productivity

256 Water samples for NPP were collected at 4-7 stations (cruise dependent) from 3-4 depths (station  
 257 dependent) from the Niskins on the CTD-rosette system during the summers of 2019 to 2022. During collection,  
 258 water was pre-filtered through 200-µm mesh (to remove mesozooplankton) into acid-washed 2-L polycarbonate  
 259 bottles. Water collection and associated incubation occurred in triplicate for surface samples at each station. Bottles  
 260 were spiked with a solution of 99% NaH<sup>13</sup>CO<sub>3</sub> (Cambridge Isotope Lab, Tewksbury, MA) for a final 10%

261 enrichment of the dissolved inorganic carbon (DIC) pool and placed in various mesh bags to simulate *in situ* light  
 262 levels. Bottles were incubated for 24 h in clear deck-board incubators with flowthrough seawater and Onset HOBO  
 263 data loggers monitored tank water temperature. At each station, the natural  $^{13}\text{C}$  in the water was determined from an  
 264 un-spiked sample and dark carbon assimilation was determined from a spiked dark bottle sample. Dark carbon  
 265 assimilation was negligible (<1%) so no correction for dark carbon assimilation was applied to this dataset.

266 The corresponding light levels at collection depths were determined using either PAR or beam attenuation  
 267 from the CTD cast for each station. When PAR data were not available (e.g., night-time casts), a relationship was  
 268 established (eq. 4) with previous daytime cast information between beam attenuation ( $c$ , measured by  
 269 transmissometer,  $\text{m}^{-1}$ ) and the light extinction coefficient ( $K_d$ ,  $\text{m}^{-1}$ ) for each cruise. During night-time casts,  $K_d$  was  
 270 estimated from the average  $c$  in the upper 10 m during the cast with the slope ( $m$ ) and intercept ( $b$ ) from the  
 271 daytime plot, according to equation 4:

$$272 \quad K_d = (m \cdot At) + b \quad (4)$$

273 The appropriate shading in incubations (%PAR) for each depth of sample collection ( $z$ ) was estimated as:

$$274 \quad \%PAR = 100e^{-K_d \cdot z} \quad (5)$$

275 At the end of each incubation, bottles were filtered under low vacuum (5-10 in. Hg) over pre-combusted  
 276 Whatman GF/F filters (450°C; 6h). Filters were stored at -20°C until further analysis on shore. NPP rates were  
 277 quantified by measuring the incorporation of isotopically heavy carbon into phytoplankton biomass. Prior to  
 278 measuring  $^{13}\text{C}$  in the samples, filters were acid fumigated with concentrated HCl in a desiccator overnight to remove  
 279 inorganic carbon. They were dried in an oven at 60°C for 24 h, individually wrapped in tin capsules and analyzed on  
 280 a Carlo Erba NC2500 elemental analyzer interfaced with a Thermo Delta V+ isotope ratio mass spectrometer. The  $\delta$   
 281  $^{13}\text{C}$  values were reported relative to the international standard Vienna PeeDee Belemnite (Coplen, 1995) and  
 282 converted to atom percent values.

283 NPP rates were calculated from atom percent values with the equation from Hama et al. (1983)

$$284 \quad NPP = \frac{POC(a_{13} - a_{ns})}{t \cdot (a_{13} - a_{ns})} \quad (6)$$

285 where NPP is the net primary production rate ( $\mu\text{g} \cdot \text{L}^{-1} \cdot \text{day}^{-1}$ ), POC is the particulate organic carbon; ( $\mu\text{g} \cdot \text{L}^{-1}$ ),  $t$  is  
 286 the incubation time (h),  $a_{13}$  is the atom % of  $^{13}\text{C}$  in the incubated sample,  $a_{ns}$  is the atom % of  $^{13}\text{C}$  in the natural  
 287 sample (un-spiked sample described above) and  $a_{ic}$  is the atom % of  $^{13}\text{C}$  in the total DIC pool. POC measurements  
 288 were blank corrected with the mean value of triplicate combusted filter blanks. The DIC concentration was  
 289 determined from salinity ( $S$ ) according to the following equation from Parsons et al. (1984):

$$290 \quad DIC = (S \cdot 0.067) - 0.05 \cdot 0.96 \quad (7)$$

291 NPP rates were integrated to the depth of the mixed layer (Table S1) to align with NCP and GOP integrated rate  
 292 calculations. The mixed layer depths were calculated from the temperature and salinity data from the CTD with the  
 293 threshold method where the mixed layer was declared to be the depth where the density difference between the  
 294 surface density and the mixed layer was greater than  $\Delta\sigma_t = 0.125 \text{ kg} \cdot \text{m}^{-3}$  (de Boyer-Montégut et al., 2004) (S3) to  
 295 align with NCP and GOP integrated rate calculations. In summer, NPP rates below 16 m (deepest mixed layer  
 296 depth) were not used in this study.

297 No discrete measurements of net primary productivity (NPP) were conducted during the summer of 2018.  
 298 However, we were able to estimate 2018 NPP rates as follows: For each summer, we computed phytoplankton  
 299 biomass production (PP,  $\text{mg} \cdot \text{C} \cdot \text{m}^{-3} \cdot \text{d}^{-1}$ ) based on surface discrete Chl- $a$  concentration and growth/grazing rates,  
 300 following the methodology outlined by Landry et al. (2003). Chl- $a$  concentrations were transformed into biomass  
 301 using a constant C:Chl- $a$  ratio of 50. In the summers from 2019 to 2022, where discrete NPP data were available, we  
 302 averaged surface PP and surface NPP by region (inner-shelf, mid-shelf, and outer-shelf) and conducted a linear  
 303 regression between these average PP and NPP rates ( $p < 0.05$ ;  $R^2 = 0.68$ ;  $n = 15$ ). The linear regression coefficient  
 304 obtained from this correlation was used to convert PP derived from growth/grazing rates in the summer of 2018 into  
 305 NPP ( $\text{mg} \cdot \text{C} \cdot \text{m}^{-3} \cdot \text{d}^{-1}$ ). Subsequently, we integrated NPP over the mixed layer to obtain integrated NPP ( $\text{mg} \cdot \text{C} \cdot \text{m}^{-2} \cdot \text{d}^{-1}$ )  
 306 at each station where surface growth/grazing rates were available. While the C:Chl ratios in coastal systems exhibit  
 307 high seasonal variability (Jakobsen and Markager, 2016), we used a constant C:Chl ratio when converting Chl- $a$  into  
 308 phytoplankton biomass. Since our comparison of derived PP was limited to the summer season, it is reasonable to  
 309 assume that C:Chl ratios remained within a similar range. Additionally, the same C:Chl ratio was used when  
 310 deriving the linear relationship and when applying it and thus the estimated NPP rates are insensitive to the choice of  
 311 C:Chl ratio. It is important to note that C:Chl ratios were not utilized in the calculation of NPP rates for any other  
 312 year.

Formatted: Subscript

Formatted: Subscript

Formatted: Font: Cambria Math

314 Mixed layer depths were confirmed to be similar when a gradient criterion with a difference of 0.0125 kg m<sup>-3</sup> was  
315 used instead (Farr et al., 2009). Primary production rates for 2018 were estimated from the growth/grazing rates.  
316 The surface values of phytoplankton growth rates were converted from Chl-a to carbon (mg C m<sup>-3</sup> d<sup>-1</sup>) with a  
317 constant ratio of 50 which was then multiplied by the mixed layer depth to get values in mg C m<sup>-2</sup> d<sup>-1</sup>.

#### 318 2.4 Autotrophic and Heterotrophic Respiration

319 Assuming a photosynthetic quotient (O:C ratio) of 1.4, respiration rates were calculated from the productivity values  
320 (GOP, NPP, and NCP) and following the relationships below:  
321

$$322 \quad \quad \quad NPP = GOP - R_A \quad \quad \quad (8)$$

$$323 \quad \quad \quad NCP = NPP - R_H \quad \quad \quad (9)$$

324 where R<sub>A</sub> is autotrophic respiration and R<sub>H</sub> is heterotrophic respiration.

325

#### 326 2.5 Growth Rates and Grazing rates

327 Rates of phytoplankton growth and protistan grazing were quantified with a 2-point modification of the dilution  
328 method (Chen, 2015; Landry et al., 2008; Chen, 2015; Morison et al., 2020) following methods in Marrec et al.  
329 (2021). Briefly, surface samples were collected at 4 to 7 stations throughout the cruise. For each sample, whole  
330 seawater (WSW) from the Niskin bottles was transferred into a 10-L polycarbonate carboy through a 200-µm mesh  
331 filter to remove mesozooplankton predators. Diluent was prepared by gravity filtration through a 0.2 µm membrane  
332 filter capsule (PALL®) from the Niskin to the carboys and mixed with WSW to obtain a 20% WSW dilution. A total  
333 of 6 bottles per experiment were prepared: 2 bottles with nutrient amended 20% WSW, 2 bottles with nutrient  
334 amended WSW, and 2 bottles with unamended WSW to assess nutrient limitation. Incubations took place for 24 h in  
335 a clear, 1m<sup>3</sup> deck-board incubator. Paired bottles were placed into mesh bags that simulated the effective light  
336 availability in the surface mixed layer, which corresponded to 65% of sea surface irradiance. Phytoplankton growth  
337 and grazing mortality rates were then estimated from changes in Chl-a over the 24 h incubation. For dilution  
338 experiments, Chl-a concentrations were obtained from triplicate 150-mL subsamples filtered on GF/F filters, after a  
339 12-h dark extraction period at room temperature in 95% ethanol and measured on a calibrated Turner 10 AU  
340 fluorometer. The full extraction method is detailed in Marrec et al. (2021).

#### 341 2.6 Discrete Chlorophyll-a sample collection and processing

342 Samples for Chl-a analysis were collected into brown amber bottles from Niskins on the CTD Rosette system. A  
343 known sample volume (250-500 mL) was filtered at low pressure (5-10 in. Hg) through either a GF/F filter or a 20  
344 µm polycarbonate Sterlitech filter. Filters were transferred to either tissue capsules (GF/F) or cryogenic vials (20  
345 µm) and then flash frozen in liquid nitrogen until extraction. Later, filters were extracted in 5 mL of 90% acetone for  
346 24 hours in a dark refrigerator, then tubes were vortexed and centrifuged (only GF/F filters), and the solution was  
347 measured on a calibrated Turner Designs Handheld Aquaflor fluorometer, acidified with 2 drops of 10%  
348 hydrochloric acid and measured again. Chl-a concentrations for different size fractions were calculated by  
349 difference. Note that in this study we consider large phytoplankton are as > 20 µm.

#### 350 2.7 Satellite and radar data

351 To look at variability in SST and surface Chl-a, a proxy for phytoplankton biomass, throughout the summers over  
352 multiple years, on a wider spatial and temporal scale than the at-sea chlorophyll data permitted, SST and surface  
353 Chl-a concentrations from remote sensing sources were retrieved and analyzed. In particular, both snapshots and  
354 monthly averages of MODIS (Moderate Resolution Imaging Spectroradiometer) SST and chlorophyll data with a  
355 horizontal resolution of 1 km were used to examine the spatial coverage of the *Hemiaulus* bloom in summer 2019  
356 (when it dominated phytoplankton biomass) and compare the surface temperature and chlorophyll in the NES region  
357 in summers 2018-2022.

Formatted: Level 2, Space Before: 12 pt, After: 12 pt

Formatted: Font: Bold, Font color: Auto

Formatted: Level 2, Space Before: 12 pt, After: 12 pt

Formatted: Font: Bold

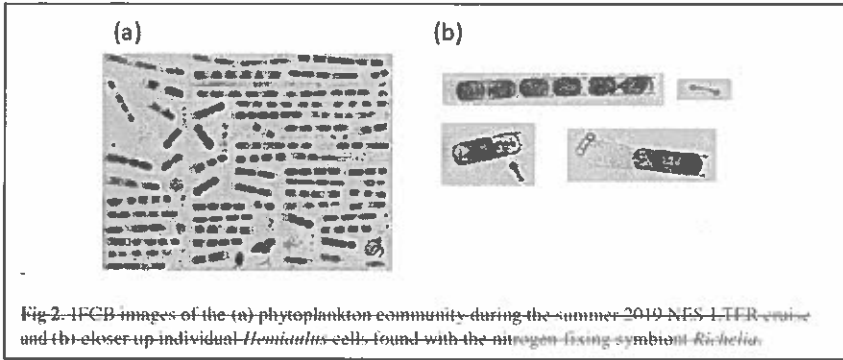
358 To examine possible origins of the bloom water, backward particle trajectory simulations were carried out  
359 with the OceanParcels Python package <https://oceanparcels.org/index.html> (Lange and van Sebille, 2017) (Lange  
360 and Van Sebille, 2017). High frequency (HF) radar-measured sea surface velocity data in the NES region in Jul-Aug  
361 2019 with 6-km spatial resolution and hourly temporal resolution were used as the background flow. Particles were  
362 released at mid-shelf sites along the NES-LTER transect on Aug 21, 2019 and advected backward for 30 days until  
363 Jul 22, 2019.

## 364 2.8 Imaging FlowCytobot

365 Composition of the phytoplankton community was assessed with Imaging FlowCytobots (IFCB; McLane Research  
366 Laboratories, Inc.). IFCB uses a combination of video and flow cytometry technology to capture images of plankton  
367 and other particles in the size range ~5-150  $\mu\text{m}$  (Olson and Sosik, 2007). During the cruises reported here, IFCB  
368 instruments were configured to record images of particles with laser-based chlorophyll fluorescence or light  
369 scattering signals above trigger thresholds and samples were pre-screened with 150  $\mu\text{m}$  Nitex. IFCB instruments  
370 were operated two ways. First, on all cruises, an IFCB was configured to sample 5 mL automatically from the ship's  
371 underway system every 25 minutes. Second, at stations occupied on the NES-LTER and SPIROPA cruises, IFCB  
372 instruments were used to analyze depth profiles from discrete samples collected with Niskin bottles. Typically, three  
373 5-mL subsamples were measured for each depth. The fraction of each 5-mL sample imaged by IFCB decreases with  
374 increasing trigger rate but is recorded precisely during sample acquisition enabling calculation of concentrations.  
375 IFCB image data were automatically analyzed following approaches developed for the IFCB time series at the  
376 Martha's Vineyard Coastal Observatory (MVCO) (Brownlee et al., 2016). In particular, cell biovolume was  
377 estimated from IFCB images (Moberg and Sosik, 2012) and converted to cell carbon following the relationships  
378 described by Menden-Deuer and Lessard (2000). IFCB images were classified with a convolutional neural network  
379 (CNN) trained to separate 155 categories of plankton and other particles observed at MVCO and across the NES  
380 region. IFCB images were classified with a convolutional neural network (CNN) (Catlett et al., 2023) trained to  
381 separate 155 categories of plankton and other particles observed at MVCO and across the NES region. We used the  
382 Inception v3 (Szegedy et al., 2016) CNN architecture as implemented in PyTorch, pre-trained with ImageNet  
383 (Russakovsky et al., 2015) and fine-tuned with an NES IFCB training set (97026 images, 155 classes, 80-20 split for  
384 training and validation). In addition, an independent test set of manually annotated images in 51 IFCB samples from  
385 EcoMon cruises was used to evaluate *Hemiaulus* quantification as a function of classifier score threshold. From this  
386 independent analysis, classifier predictions with scores above 0.9 performed very well for *Hemiaulus* (class-specific  
387 F1-score = 0.936; CNN-count vs. manual-count:  $r^2 = 0.999$ , slope = 0.915; intercept = 0.005).

## 388 2.9 Nutrients

389 Dissolved inorganic nutrient concentrations (ammonium, phosphate, silicate, and nitrate + nitrite) were obtained  
390 from CTD bottle samples with duplicates. Seawater was passed through an EMD Millipore sterile Sterivex 0.22  $\mu\text{m}$   
391 filter with filtrate collected into acid-washed 20-ml scintillation vials (after triplicate rinses), which were then stored  
392 at -20  $^{\circ}\text{C}$  until analysis. Samples were processed at Woods Hole Oceanographic Institution's Nutrient Analytical  
393 Facility with a four-channel segmented flow SEAL AA3 HR Autoanalyzer. Detection levels are as follows: 0.01  
394  $\mu\text{mol L}^{-1}$  for silicate, 0.03  $\mu\text{mol L}^{-1}$  for phosphate, 0.04  $\mu\text{mol L}^{-1}$  for nitrate + nitrite, and 0.03  $\mu\text{mol L}^{-1}$  for  
395 ammonium.



398 **Results**

399 **3.1 *Hemiaulus* distribution and**  
400 **Chlorophyll**

401 During the NES-LTER summer 2019 cruise,  
402 through automated image classification and  
403 analysis and through visual microscopic

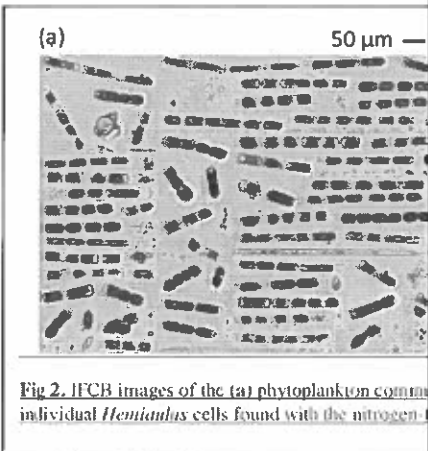


Fig 2. IFCB images of the (a) phytoplankton community and (b) closer-up individual *Hemiaulus* cells found with the nitrogen-fixing symbiont *Richetia*.

404 confirmation, a bloom of the diatom genus  
405 *Hemiaulus* was observed in the surface  
406 waters of the mid-shelf region (Fig. 2a).  
407 These images also showed N<sub>2</sub> fixing  
408 symbionts, namely *Richetia*, inside or next to

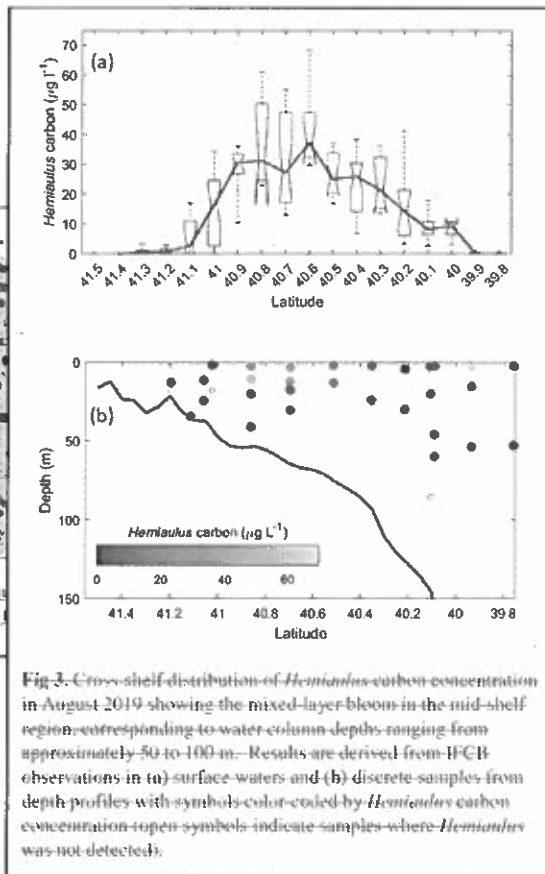


Fig 3. Cross-shelf distribution of *Hemiaulus* carbon concentration in August 2019 showing the mixed-layer bloom in the mid-shelf region corresponding to water column depths ranging from approximately 50 to 100 m. Results are derived from IFCB observations in (a) surface waters and (b) discrete samples from depth profiles with symbols color-coded by *Hemiaulus* carbon concentration (open symbols indicate samples where *Hemiaulus* was not detected).

409 the *Hemiaulus* cells (Fig. 2b).  
 410 Additionally, *Hemiaulus* carbon was  
 411 highest in the mid-shelf waters between  
 412 latitudes of 40.1° N and 41.1° N, a span of  
 413 111 km (Fig. 3a), with concentrations  
 414 ranging from 6.8 to 68.3  $\mu\text{g L}^{-1}$ . This  
 415 bloom was only observed in the surface  
 416 waters of the mid-shelf region, as can be  
 417 seen by discrete IFCB measurements from  
 418 Niskin samples (Fig. 3b). *Hemiaulus*  
 419 carbon concentrations observed in other  
 420 years on NES-LTER transect cruises never  
 421 reached values above 0.30  $\mu\text{g L}^{-1}$ —so  
 422 approximately two orders of magnitude  
 423 smaller than was observed on the 2019  
 424 cruise. Furthermore, IFCB-based  
 425 observations made on a broader scale from  
 426 the mid-Atlantic bight to the Gulf of Maine  
 427 in the period from 2013 to 2023, show that  
 428 only in August 2019 is *Hemiaulus* present  
 429 in large quantities (Fig. S1), confirming the  
 430 extraordinary nature of the 2019 bloom.  
 431 The presence of the diatom bloom  
 432 was consistent with the size-fractionated  
 433 Chl-a data. Surface Chl-a concentrations in  
 434 the mid-shelf region in summer are  
 435 typically low ( $< 0.50 \mu\text{g L}^{-1}$ , Fig. 4a) and  
 436 progressively decrease with decreasing  
 437 latitude. However, during the 2019  
 438 NES-LTER summer cruise, however, Chl-a  
 439 concentrations were observed up to as high  
 440 as  $3.50 \mu\text{g L}^{-1}$  in the surface waters of the  
 441 mid-shelf (mean Chl-a of  $1.9697 \mu\text{g L}^{-1}$ ,  
 442 Table 2) with up to 80% of the Chl-a  
 443 associated with the  $> 20 \mu\text{m}$  fraction (Fig.  
 444 4c). This is in contrast to other summers

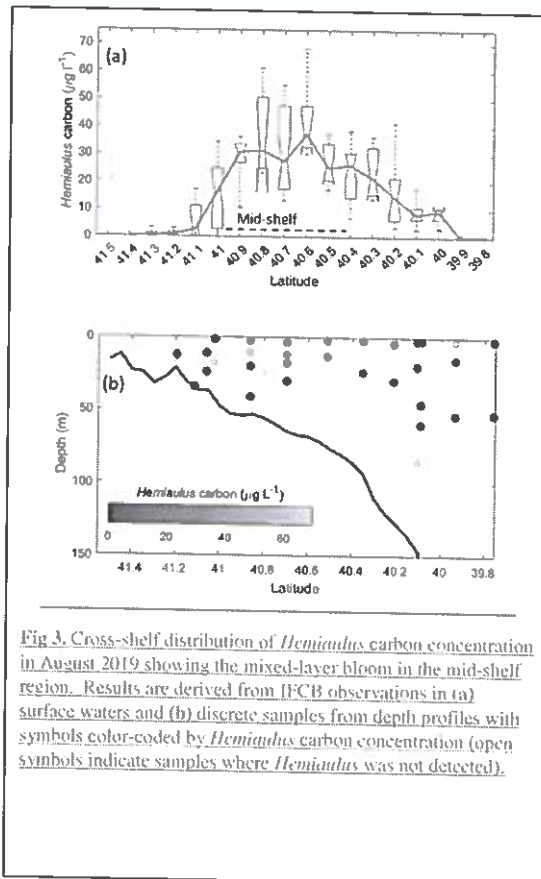


Fig 3. Cross-shelf distribution of *Hemiaulus* carbon concentration in August 2019 showing the mixed-layer bloom in the mid-shelf region. Results are derived from IFCB observations in (a) surface waters and (b) discrete samples from depth profiles with symbols color-coded by *Hemiaulus* carbon concentration (open symbols indicate samples where *Hemiaulus* was not detected).

445 when most of the Chl-a was  
 446 associated with the < 20  $\mu\text{m}$   
 447 fraction (Fig. 4b, d-f).  
 448 Concentrations of Chl-a in the >  
 449 20  $\mu\text{m}$  size fraction and  
 450 concentrations of *Hemiaulus*  
 451 carbon in the NES-LTER  
 452 summer 2019 cruise were larger  
 453 at co-located sampling locations  
 454 in the beginning of the cruise  
 455 than at the end, suggesting that  
 456 the bloom may have peaked  
 457 before the cruise started and thus  
 458 was in decline during the cruise  
 459 period.

460 Monthly mean surface  
 461 Chl-a concentrations from  
 462 remote sensing were used to  
 463 investigate if the observed  
 464 differences in Chl-a and  
 465 productivity between the  
 466 summers were related to  
 467 differences in the timing of the  
 468 cruise as opposed to differences  
 469 in community composition  
 470 (Fig. S1S3). In many of the

471 summers (2018, 2021, and 2022), Chl-a in July was actually higher than in August, suggesting that the timing of the  
 472 2019 cruise (end of August instead of end of July) was not a factor in explaining the anomalous results. In 2019, in  
 473 situ observations from both July and August confirm the conclusion from the satellite data that the transect area had  
 474 larger Chl-a concentrations in August than in July. In particular, a patch of high chlorophyll in the mid-shelf  
 475 between 40.2°N and 40.7°N to the immediate west of the transect was present in August 2019, likely resulting from  
 476 the observed *Hemiaulus* bloom anomalously high productivity observed in August, 2019. If anything, the change in  
 477 timing of the 2019 NES-LTER cruise would lead us to expect the Chl-a to be lower in August than in July and thus  
 478 the high Chl-a observed in August, 2019 is even more startling. Satellite data cannot be used to confirm the presence  
 479 or absence of *Hemiaulus*. However, JFCB data from NES broadscale NOAA EcoMon surveys from summer 2013 to  
 480 2023, many of which occurred in August, always showed minimal presence of *Hemiaulus*, suggesting the observed  
 481 bloom in August 2019 was indeed extraordinary and not simply related to the timing of the 2019 LTER cruise (Fig.  
 482 S1).  
 483  
 484

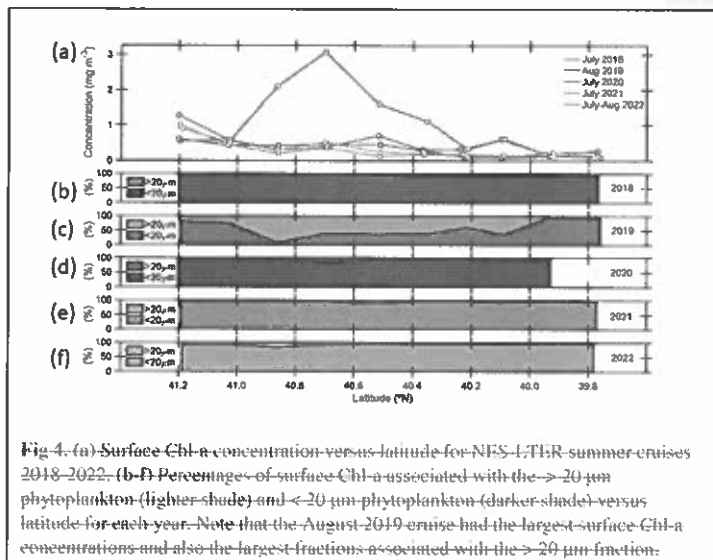


Fig. 4. (a) Surface Chl-a concentration versus latitude for NES-LTER summer cruises 2018–2022. (b–f) Percentages of surface Chl-a associated with the > 20  $\mu\text{m}$  phytoplankton (lighter shade) and < 20  $\mu\text{m}$  phytoplankton (darker shade) versus latitude for each year. Note that the August 2019 cruise had the largest surface Chl-a concentrations and also the largest fractions associated with the > 20  $\mu\text{m}$  fraction.

Formatted: Font: Not Bold, Font color: Auto

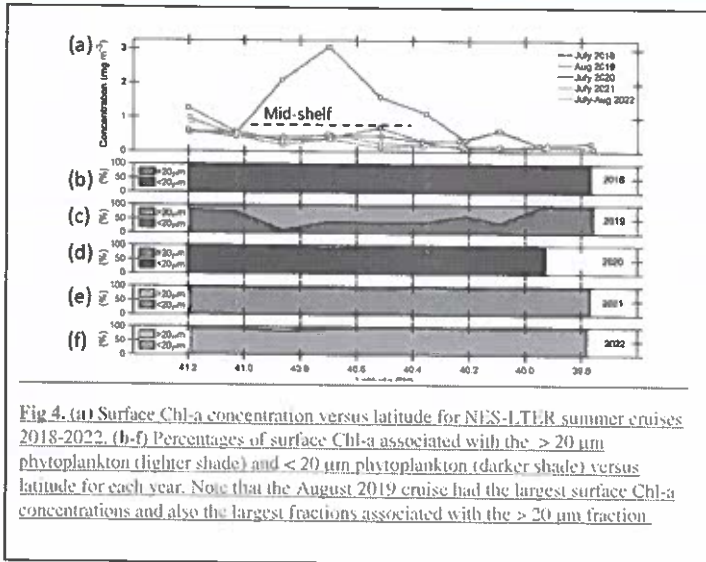


Fig 4. (a) Surface Chl-a concentration versus latitude for NES-LTER summer cruises 2018-2022. (b-f) Percentages of surface Chl-a associated with the > 20 μm phytoplankton (darker shade) and < 20 μm phytoplankton (lighter shade) versus latitude for each year. Note that the August 2019 cruise had the largest surface Chl-a concentrations and also the largest fractions associated with the > 20 μm fraction.

### 485 3.2 Physical properties

486 During the NES-LTER summer 2019 cruise, SST was in the mid-shelf region, was only slightly higher than during  
 487 most of the other summer cruises in the mid-shelf region (Table 2). Furthermore, Fig. 5). In contrast, SST in  
 488 summer 2019 on the outer-shelf region in particular was substantially higher than on any other summer cruise (Fig.  
 489 5a6a). Notably, the 2019 cruise occurred later in the summer season (August) than the NES-LTER cruises in other  
 490 years (July). Along the NES-LTER transect specifically, SST in July 2019 was lower than in August 2019 and was  
 491 similar to other years. In general, monthly-averaged satellite SST data in the broader NES region usually  
 492 show showed lower SST values in July compared to August (2018, 2020-2022) (Fig. S2S3). Interestingly, however,  
 493 in summer 2019, the monthly averaged satellite data actually shows showed higher SST in July, because of  
 494 impingement of a Gulf Stream warm-core ring on the shelf edge (Zhang et al., 2023) and the subsequent onshore  
 495 intrusion of the ring water in July 2019. The fact that monthly averaged satellite SST was higher in July than August  
 496 but the local NES-LTER transect data show had higher temperature higher in August than July suggests that the  
 497 high SST observed during late August 2019 reflected an ephemeral event and not a mean condition during that  
 498 month. Despite the occurrence of the NES-LTER summer 2019 cruise during a specific week of August and  
 499 conditions that suggest an ephemeral event, for simplicity, we will refer to it as August 2019 in this paper. During  
 500 the NES-LTER August 2019 cruise, surface salinity was lower than on 2018, 2021, and 2022 summer cruises, but  
 501 similar to surface salinity during the July 2020 cruise (Fig. 5b5, Fig. 6b) and to salinities observed in July 2019  
 502 along the NES-LTER transect. Despite the NES-LTER summer 2019 cruise being in a specific week of August and  
 503 the conditions suggesting an ephemeral event, for simplicity, we will refer to it as August 2019 in this paper.  
 504

Formatted: Font color: Black



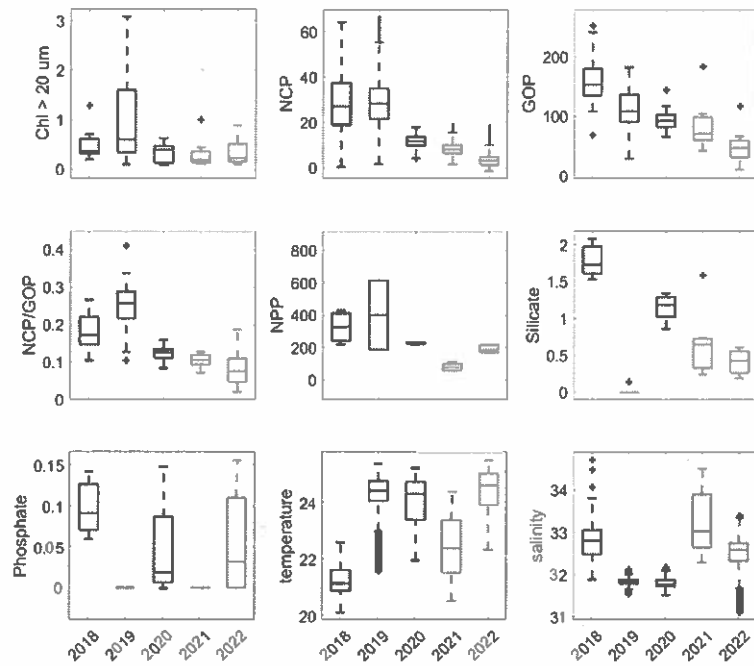
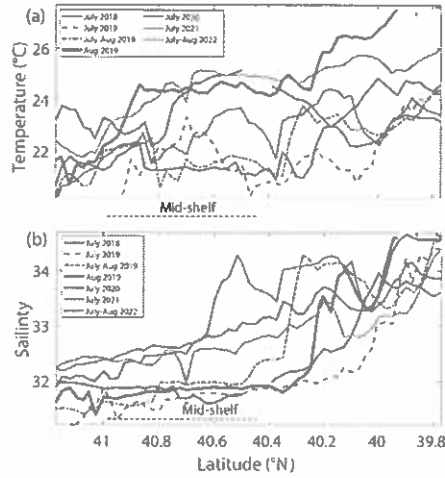
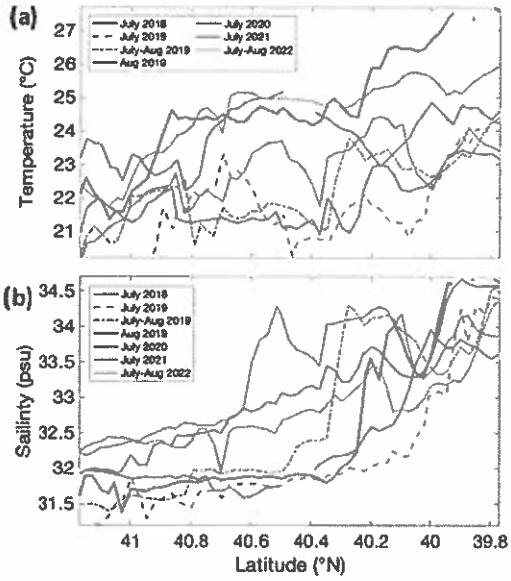


Fig. 5. Box plots of data in the summer, mid-shelf region for a) chlorophyll associated with cells > 20 μm in units of  $\text{mg m}^{-3}$ , b) net community production (NCP) and c) gross oxygen production (GOP) both in units of  $\text{mmol O}_2 \text{ m}^{-2} \text{ d}^{-1}$ , d) NCP/GOP (unitless) which is a measure of export efficiency, e) Net Primary Production (NPP) in units of  $\text{mg C m}^{-2} \text{ d}^{-1}$ , f) silicate and g) phosphate, both in units of  $\mu\text{mol L}^{-1}$ , h) sea surface temperature in degrees Celsius and i) salinity in psu. These plots show the differences in the plotted variables that occurred in August 2019 (orange box in each plot), a year when *Hemiaulus* carbon equaled  $28.4 \mu\text{g L}^{-1}$ , compared to the data from the other summers, all of which had *Hemiaulus* carbon  $<0.02 \mu\text{g L}^{-1}$ .

**Table 2.** Averages  $\pm$  standard errors, standard deviations, and number of measurements (n) of surface mixed layer characteristics (productivity values integrated through the surface mixed layer; physical conditions, nutrients, and Chl-a concentrations from the surface) in the mid-shelf region (70.883° W, 40.437° N + 40.980° N, water depth 50 to 100 m) measured during NES-LTER summer cruises for each year and over all averages from. The last columns show the mean data for winter NES-LTER water cruises 2018-2022 in the same mid-shelf waters of the transect region. The NPP average in 2018 (\*) was calculated based on the phytoplankton growth rate since direct NPP measurements were not available for this year. The standard error for 2020 NPP reflects the replicate values from one station rather than multiple mid-shelf stations. The winter averages reflect mean of data collected in winters of 2018-2022 - see text for details.

	2018			2019			2020			2021			2022			All winters		
	mean	std	n	mean	std	n	mean	std	n	mean	std	n	mean	std	n	mean	std	n
NCP (mmol C m <sup>-3</sup> d <sup>-1</sup> )	28.8	1.60	6	28.8	1.72	6	28.8	1.72	6	28.8	1.72	6	28.8	1.72	6	28.8	1.72	6
chl-a (µg m <sup>-3</sup> )	0.19	0.19	4	0.17	0.17	4	0.17	0.17	4	0.17	0.17	4	0.17	0.17	4	0.17	0.17	4
Temperature (°C)	21.44	0.20	2	21.44	0.20	2	21.44	0.20	2	21.44	0.20	2	21.44	0.20	2	21.44	0.20	2
Salinity (psu)	34.9	0.1	4	34.9	0.1	4	34.9	0.1	4	34.9	0.1	4	34.9	0.1	4	34.9	0.1	4
Hydrophobic Carbon (µg l <sup>-1</sup> )	0.002	0.002	4	0.002	0.002	4	0.002	0.002	4	0.002	0.002	4	0.002	0.002	4	0.002	0.002	4
Chl-a (µg m <sup>-3</sup> )	0.02	0.02	4	0.02	0.02	4	0.02	0.02	4	0.02	0.02	4	0.02	0.02	4	0.02	0.02	4
Water pH	8.1	0.1	4	8.1	0.1	4	8.1	0.1	4	8.1	0.1	4	8.1	0.1	4	8.1	0.1	4
Silicate (µmol l <sup>-1</sup> )	0.11	0.11	4	0.11	0.11	4	0.11	0.11	4	0.11	0.11	4	0.11	0.11	4	0.11	0.11	4
Phosphate (µmol l <sup>-1</sup> )	0.025	0.025	4	0.025	0.025	4	0.025	0.025	4	0.025	0.025	4	0.025	0.025	4	0.025	0.025	4

Deleted Cells	... [1]
Deleted Cells	... [2]
Inserted Cells	... [14]
Inserted Cells	... [20]
Inserted Cells	... [23]
Formatted	... [3]
Formatted	... [4]
Formatted	... [6]
Inserted Cells	... [15]
Inserted Cells	... [16]
Inserted Cells	... [17]
Formatted	... [5]
Formatted	... [12]
Formatted	... [18]
Formatted	... [9]
Inserted Cells	... [41]
Inserted Cells	... [47]
Inserted Cells	... [54]
Inserted Cells	... [65]
Split Cells	... [24]
Formatted	... [25]
Deleted Cells	... [27]
Formatted	... [28]
Deleted Cells	... [31]
Inserted Cells	... [60]
Inserted Cells	... [64]
Formatted	... [38]
Formatted	... [42]
Formatted	... [48]
Formatted	... [55]
Formatted	... [61]
Formatted	... [51]
Formatted	... [43]
Formatted	... [62]
Formatted	... [36]
Formatted	... [37]
Formatted	... [56]
Formatted	... [29]
Formatted	... [44]



516  
517  
518  
519  
520  
521  
522  
523  
524  
525  
526  
527  
528  
529  
530  
531  
532  
533  
534

Fig 56. (a) Temperature and (b) salinity 5 m below the surface versus latitude for NES-LTER summer cruises (2018-2022) and the SPIROPA and OTZ summer 2019 cruises. For clarity, the values are averaged in 0.025 degree latitude bands when there were multiple occupations of the same region. The mid-shelf region is denoted by a dashed line.

Formatted: Font: 10 pt

Formatted: Left

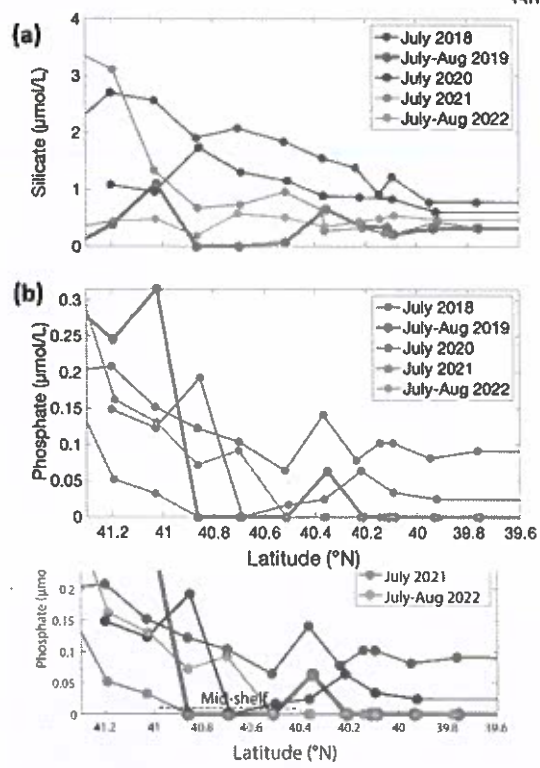


Fig 67. (a) Silicate and (b) phosphate concentrations (in  $\mu\text{mol/L}$ ) in the upper 12 m of the water column for NES-LTER summer cruises (2018-2022). The mid-shelf region is denoted by a dashed line.

562

### 563 3.3 Nutrients

564 Nutrient concentrations differed between the August 2019 cruise and other summer cruises. Specifically, phosphate  
 565 and silicate concentrations in surface waters were lower in August 2019 compared to most other summers (Table 2,  
 566 Fig. 5, Fig. 7). In other summers, silicate decreased with distance from shore, but in 2019, silicate was depleted  
 567 between 41°N and 40.4°N (Fig. 6a7a) coincident with the location of the *Hemiaulus* bloom. Additionally, higher  
 568 levels of silicate were found around depths of 50 m to 140 m in August 2019 than during other summer NES-LTER  
 569 cruises (Fig. 6a7a), which may be associated with diatoms that had sunk and were starting to be remineralized,  
 570 releasing silicate back into the water column. Surface water phosphate concentrations in August 2019 were depleted  
 571 south of 41°N (Fig. 6b7b). However, low concentrations of phosphate were also found in summersummer of 2020  
 572 and 2021. Lastly, while nitrate plus nitrite were measured on the same samples as phosphate and silicate, nitrate +  
 573 nitrite concentrations were close to the detection level in the surface samples for all summer cruises except a few  
 574 stations in 2018, and thus are not shown here. Ammonium levels are not discussed because the samples were frozen  
 575 at sea and thus may not be reliable; additionally, ammonium levels showed no clear relationship over the transect  
 576 cruises.  
 577

### 578 3.4 Productivity and grazing rates

579 In August 2018 NCP was  
 580 elevated in the mid-shelf waters,  
 581 coincident with the location of the  
 582 *Hemiaulus* bloom (Fig. 1). NCP  
 583 peaked in the first half of the  
 584 cruise and decreased during the  
 585 second half, supporting the earlier  
 586 supposition that the *Hemiaulus*  
 587 bloom was likely in decline. (Fig.  
 588 S2). Additionally, the area of  
 589 maximum NCP moved shoreward  
 590 in the second half of the cruise.  
 591 The high NCP was primarily  
 592 constrained to the main longitude  
 593 sampling line and usually did not  
 594 extend, at least at those points in  
 595 time, spatially off the main  
 596 transect.

597 During August 2019,  
 598 waters with high carbon  
 599 concentrations of *Hemiaulus*  
 600 showed higher rates of NCP (Fig.  
 601 7a8a), NCP/GOP (Fig. 7b8b),  
 602 GOP (Fig. 7c8c), and NPP (Fig.  
 603 7d8d) compared to these rates at  
 604 mid-shelf waters in most other  
 605 years. (Fig. 5). More specifically,  
 606 the mid-shelf waters where  
 607 *Hemiaulus* was present in Aug  
 608 2019 displayed NCP values  
 609 approximately 2.5 to 9 times  
 610 larger than in the same mid-shelf  
 611 latitudes in summers of 2020-22  
 612 (Table 2). Furthermore, we

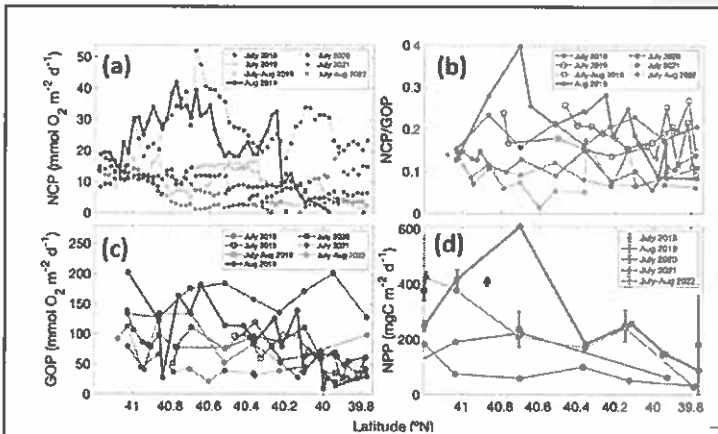


Fig. 7. (a) NCP, (b) NCP/GOP, and (c) GOP rates integrated throughout the mixed layer for NES-LTER summer cruises (2018-2022) and SPR/GPA and OTZ summer 2019 cruises. Values are averaged in 0.025-degree latitude bands to average multiple occupations of the same region. The same overall pattern are seen with and without the averaging within these latitude bands. (d) Average NPP value, integrated to the bottom of the mixed layer for NES-LTER summer cruises (2019-2021) with error bars reflecting the standard deviation of triplicate surface water incubation. NPP values were not directly measured for summer 2018 but were instead estimated from phytoplankton growth rate in the grazing incubation experiments (black circles). were not directly measured for summer 2018 but were instead estimated from phytoplankton growth rate in the grazing incubation experiments (black circles). The mid-shelf region is denoted by a dashed line.

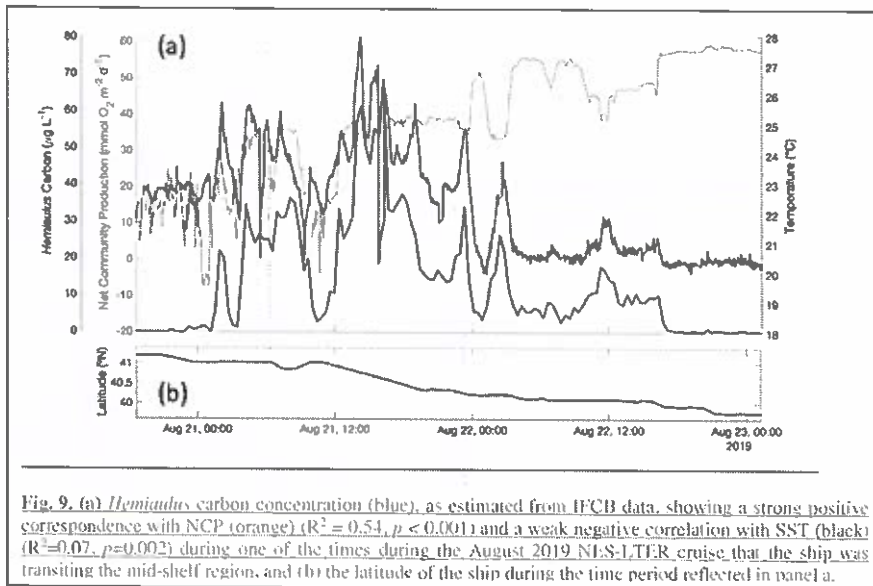


Fig. 9. (a) *Hemiaulus* carbon concentration (blue), as estimated from IFCB data, showing a strong positive correspondence with NCP (orange) ( $R^2 = 0.54$ ,  $p < 0.001$ ) and a weak negative correlation with SST (black) ( $R^2 = 0.07$ ,  $p = 0.002$ ) during one of the times during the August 2019 NIS-LEER cruise that the ship was transiting the mid-shelf region, and (b) the latitude of the ship during the time period reflected in panel a.

613 observed a correlation between NCP and *Hemiaulus* carbon between Aug 21 and Aug 23 (Fig. 89;  $R^2 = 0.54$ ,  $p <$   
 614  $0.001$ ). The patchiness of the diatom bloom corresponded to the patchiness in NCP. Additionally, one can see that  
 615 the cooler shelf water was associated with higher abundances of *Hemiaulus* than the warmer slope water (Fig. 89),  
 616 suggesting a water mass dependence on the location of the *Hemiaulus* bloom. Thus, the patchiness in the bloom and  
 617 NCP is likely a result of the ship crossing different water masses.  
 618 GOP rates were only slightly higher in summer 2019 than in other summers (Fig. 5 and 8c). In particular,  
 619 GOP rates were higher by a factor of 1.1 in waters with the *Hemiaulus* bloom in 2019 than during the summers of  
 620 2020-21; GOP rates were much higher in August 2019 than in summer of 2022 by a factor of 2.75. Additionally,  
 621 during August 2019, NPP, NCP, GOP, and NCP/GOP rates in summer 2018 were generally higher  
 622 throughout the cruise compared to these rates from July 2020– in August 2019 (discussed below in  
 623 section 4.1).

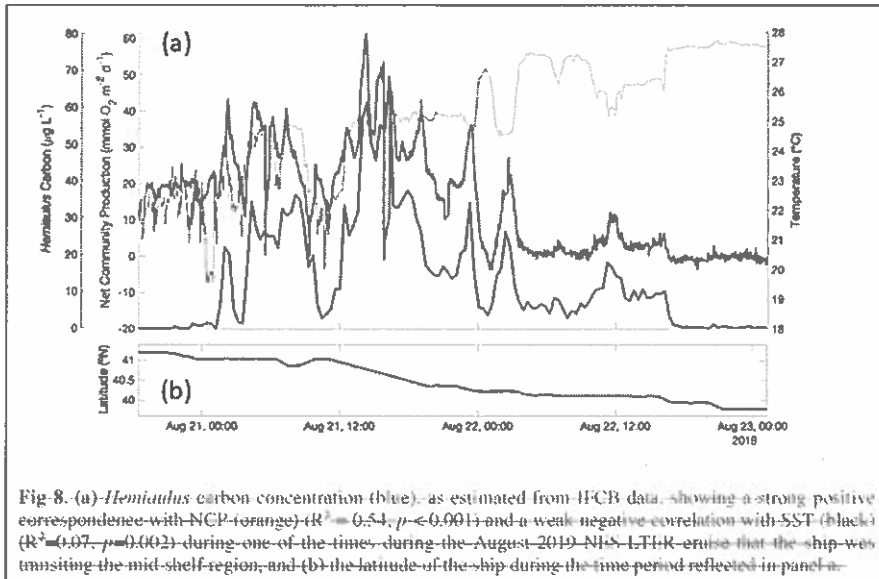


Fig. 8. (a) *Hemiaulus* carbon concentration (blue) as estimated from IFCB data, showing a strong positive correspondence with NCP (orange) ( $R^2 = 0.54$ ,  $p < 0.001$ ) and a weak negative correlation with SST (black) ( $R^2 = 0.07$ ,  $p = 0.002$ ) during one of the times during the August 2019 NES-LLTER cruise that the ship was transiting the mid-shelf region, and (b) the latitude of the ship during the time period reflected in panel a.

624 Additionally, within 2022 and estimates for July 2018. Within the region that corresponds directly with the  
 625 location of the *Hemiaulus* bloom, NPP rates in 2019 were ~1.5 - 2.5 times higher than NPP rates during other  
 626 summer cruises. (Fig. 7d8d; Table 2). More specifically, NPP at 40.7  $^{\circ}\text{N}$  was approximately double the NPP  
 627 measured in 2020 and more than double the rate measured in 2021. Furthermore, at 40.4  $^{\circ}\text{N}$ , NPP in 2019 was about  
 628 40% higher than in 2021 (no data for this station in 2020) (Fig. 7d78d).

629 A larger difference between NCP in the various summers than between GOP in the summers suggests that  
 630 the increase in NCP in August 2019 was due to both increased photosynthesis and decreased community respiration.  
 631 As a first approach through approximation, we calculated autotrophic respiration and heterotrophic respiration to  
 632 show that autotrophic respiration was lower than average in August 2019 ( $R_A = 308 \text{ mgC mg C m}^{-2} \text{ d}^{-1}$  in August 2019  
 633 versus 496  $\text{mgC m}^{-2} \text{ d}^{-1}$  average for the other summers). This approach also showed that heterotrophic respiration was  
 634 higher than average in August 2019 (431  $\text{mgC m}^{-2} \text{ d}^{-1}$  in August 2019 versus 247  $\text{mgC mg C m}^{-2} \text{ d}^{-1}$  average for the  
 635 other summers). Note this estimation is highly uncertain due to the different time and spatial scales associated with  
 636 the gas tracers used to quantify NCP, and GOP, and NCP/GOP rates in summer 2018 were comparable to these  
 637 rates in August 2019 (discussed below in section 4.1) and the incubation techniques used for NPP.

638 Since the summer 2019 NES-LLTER cruise occurred in the middle of August rather than in mid to late July  
 639 as was typical for most other summers, the physical conditions were inherently different in 2019. We compared  
 640 NCP and GOP data (NPP not available) from two earlier cruises in summer 2019 (cruise details in Table 1) whose  
 641 stations/cruise track in the mid-shelf region overlapped with those of the LLTER cruise (Fig. 7), i.e. followed the  
 642 same longitude 70.883  $^{\circ}\text{W}$ . These cruises occurred before the *Hemiaulus* bloom and while their IFCB records did not  
 643 show high showed a detection of *Hemiaulus*, the abundance of *Hemiaulus* this diatom was very low ( $< 1 \mu\text{gC L}^{-1}$ ),  
 644 although it was detected at that time. These two July 2019 cruises had much lower NCP rates compared to August

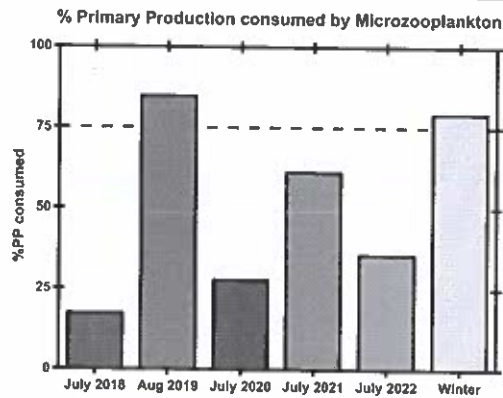


Fig. 10. Percentage of primary production (%PP) consumed by microzooplankton in surface waters in the mid-shelf region during NES-LTER cruises for each summer and the overall average from NES-LTER winter cruises 2018-2022. %PP consumed by microzooplankton is calculated as the ratio of microzooplankton grazing rate ( $d^{-1}$ ) to phytoplankton growth rate ( $d^{-1}$ ).

645 2019 NCP rates, and specifically with had rates similar to those observed in summer 2020-22 NES-LTER transect  
 646 cruises (Fig. 7a & b). Together, these data suggest that higher production rates in 2019 were uniquely tied to the  
 647 presence of *Hemiaulus* rather than representing deviations in timing or environmental conditions.  
 648 The ratio of protistan grazing to phytoplankton growth rates provides an estimate of the percent of primary  
 649 production (%PP) consumed by microzooplankton (Fig. 910). In contrast to typical summer conditions ( $> 0.6 d^{-1}$ ,  
 650 Table 2), during August 2019, phytoplankton growth rates during the *Hemiaulus* bloom were low ( $< 0.2 d^{-1}$ , Table  
 651 2), likely because the bloom was near its end, with most of the primary production consumed by microzooplankton  
 652 (%PP = 84%, Table 2). Thus in August 2019, the) compared to other summers, with most of the primary production  
 653 consumed by microzooplankton (%PP = 84%, Table 2). Notably, these low phytoplankton growth rates are in the  
 654 same range as other diatoms with *Richelia* symbionts, namely  $0.3 d^{-1}$  for *Rhizosolenia-Richelia* cultured at a similar  
 655 temperature (Villareal, 1990). Thus in August 2019, phytoplankton growth and microzooplankton grazing were  
 656 well coupled (though only in the part of the transect where *Hemiaulus* bloomed), like typical winter conditions,  
 657 when the phytoplankton community structure is dominated by large cells, instead of the decoupling typically



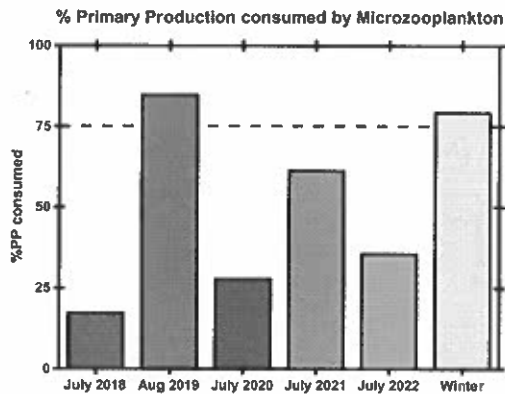


Fig. 9. Percentage of primary production (%PP) consumed by microzooplankton in surface waters in the mid-shelf region during NES-LTER cruises for each summer and the overall average from NES-LTER winter cruises 2018-2022. %PP consumed by microzooplankton is calculated as the ratio of microzooplankton grazing rate ( $d^{-1}$ ) to phytoplankton growth rate ( $d^{-1}$ ).

658 observed in most summer conditions dominated by picoplankton (Marrec et al., 2021). We note that coupling  
 659 between phytoplankton growth and microzooplankton grazing was occasionally observed during other summer  
 660 cruises, but mostly in inner-shelf waters (except one mid-shelf station in July 2021). Overall, most of the primary  
 661 production during the *Hemiaulus* bloom was grazed by microzooplankton indicating high trophic transfer efficiency  
 662 from phytoplankton to microzooplankton.

#### 663 4 Discussion

##### 664 4.1 Change in community composition altering biological rates

665 A bloom of *Hemiaulus* has not been observed on any previous NES-LTER cruise and to our knowledge,  
 666 has not been reported in the broader NES region before. Additionally, only in August 2019, compared to summers  
 667 2018 and 2020-22, was most of the Chl-a was associated with the  $> 20 \mu m$  size fraction. Thus, the presence of the  
 668 diatom bloom found in August 2019 was a major change in phytoplankton composition observed in this region of  
 669 the NES that likely led to the observed large changes in productivity rates and the coupling between  
 670 phytoplankton growth and grazing.

671 It is likely that the nitrogen-fixing symbionts in *Hemiaulus* allowed the diatom to thrive in the stratified,  
 672 low nutrient surface waters of the summer shelf. This is supported by phosphate being drawn down to levels  
 673 below detection only in August 2019; the nitrogen-fixing symbionts in the *Hemiaulus* likely made phosphate a  
 674 limiting factor for growth (Tang et al., 2020) in August 2019 whereas nitrate limitation is typical for NES summer  
 675 conditions. Additionally, while the summer of 2021 also had very low phosphate, summer 2021 was  
 676 different in that it also had low productivity rates and more typical levels of silicate, suggesting the low phosphate  
 677 occurred for fundamentally different reasons in 2019 and 2021.

678 Silicate is especially important for diatoms because it is required for formation of their cell frustules.  
 679 Moreover, previous studies show that the availability of dissolved silica seems to be an important control for many  
 680 diatom-diazotroph blooms by affecting the growth rate and size of the diatom's frustules (Kemp and Villareal, 2013;  
 681 Spitzer, 2015). The observed depletion of silicate and phosphate in the surface water during the August 2019 cruise  
 682 suggests that, at the time of the cruise, the *Hemiaulus* bloom might have been on the decline. The very low  
 683 phytoplankton growth rates might also support the idea that the bloom had peaked but also might be attributed to the  
 684 inverse relationship between phytoplankton cell size and growth rate (e.g. Finkel et al., 2010). The higher levels of

Formatted: Font color: Black

685 silicate observed at depth in August 2019 are likely due to the *Hemiaulus* sinking out of the euphotic zone and their  
686 frustules re-mineralizing (Kemp and Villareal, 2013; Spitzer, 2015). The observed depletion of silicate and  
687 phosphate in surface waters during the August 2019 cruise suggests that, at the time of the cruise, the *Hemiaulus*  
688 bloom may have been in decline. The low phytoplankton growth rates of  $0.2 \text{ day}^{-1}$  support the idea that the bloom  
689 had peaked, particularly given the fact that with sufficient phosphate, silicate and light, the *Hemiaulus* DDA can  
690 achieve growth rates of  $0.7\text{-}0.9 \text{ d}^{-1}$  in laboratory cultures (Pyle et al., 2020). Low growth rates also could be  
691 attributed to the inverse relationship between phytoplankton cell size and growth rate. The *Hemiaulus* population  
692 could have been limited by phosphate, silicate, or both. The higher levels of silicate observed at depth in August  
693 2019 are likely due to *Hemiaulus* sinking out of the euphotic zone and frustule remineralization at depth, which  
694 would release the silicate and other nutrients back into the water (Twining et al., 2014). In any case, it appears the  
695 *Hemiaulus* population could have been limited by phosphate, silicate, or both.

696 The strong coherence between the high spatial resolution data on *Hemiaulus* carbon concentrations and  
697 NCP (Fig. 89), as well as the other data presented here and a clear potential mechanism, strongly support the idea  
698 that the high productivity rates observed in August 2019 are directly due to the presence of *Hemiaulus*. In particular,  
699 the high NCP rates observed during the August 2019 NES-LTER cruise and their overlap with the location of the  
700 diatom bloom, suggest a high export ecosystem developed due to *Hemiaulus*' influence on productivity and  
701 biological rates. Here, we are defining export as a flux away from the local biological production  
702 compartment, which can include losses of carbon (or oxygen) to depth or transfer to higher trophic levels. While the  
703 *Hemiaulus* bloom slightly increased total photosynthesis, as seen from the GOP rates, the bloom presence affected  
704 NCP, and thus by extension, export production—even more to a higher degree, potentially due to the large size of  
705 *Hemiaulus* cells and chains. The NCP/GOP ratio in August 2019 was double the ratio observed in the summers  
706 2020-22 (Table 2, Fig. 5). Other studies have shown links between variations in NCP/GOP and changes in  
707 planktonic community composition (Palevsky et al., 2016). Bigger phytoplankton cells sink faster than small ones,  
708 making them less likely to be grazed before sinking out of the euphotic zone, allowing for a higher export efficiency.  
709 Additionally, a higher trophic transfer efficiency (see next paragraph) would also lead to a larger NCP/GOP ratio.  
710 Hence, the NES-LTER summer of 2019 cruise appears to represent have represented a high carbon export efficiency  
711 system.

712 Not only did NCP and GOP rates change because of the *Hemiaulus* bloom, but so did NPP, phytoplankton  
713 growth rates, chl-a concentrations, and the trophic transfer efficiency within the planktonic food web. The presence  
714 of *Hemiaulus* in the mid-shelf region likely led to the observed higher NPP rates during August 2019 compared to  
715 all other observed summers in the mid-shelf region of the NES (Fig. 75 and 8). High NPP rates associated with  
716 diatom blooms have been observed in other systems such as on the Eastern Bering Shelf (Lomas et al., 2012) and in  
717 the Gulf of California (Puigcorbe et al., 2015)—in particular, including during blooms of diatom-diazotroph  
718 associations such as *Hemiaulus-Richelia* are known to significantly increase NPP (Gaysina et al., 2019). For  
719 example, Tang et al. (2020) reported a high contribution of nitrogen fixation to NPP off the coast of New Jersey  
720 during their 2015-2016 survey in the Western North Atlantic. Even though high NPP was associated with the  
721 location of the *Hemiaulus* bloom in our study, phytoplankton growth rates were low ( $< 0.2 \text{ d}^{-1}$ ). This decoupling  
722 between NPP and growth was likely due to the order of magnitude higher chl-a concentrations observed during  
723 August 2019 ( $1.37 \mu\text{g L}^{-1}$ ) compared to other summers ( $0.01 - 0.03 \mu\text{g L}^{-1}$ ; Table 2) since NPP is roughly the  
724 product of phytoplankton growth and biomass (Marchetti et al. 2009). Thus, although growth rate was low, biomass  
725 was so high that NPP was also high. Furthermore, most of the primary production was directly consumed by  
726 microzooplankton, which we have not observed during any other summer NES-LTER cruise, suggesting the  
727 presence of *Hemiaulus* led to more efficient trophic transfer during August 2019. While conditions with high NCP  
728 (i.e. low community respiration) and high grazing pressure as observed in August 2019 may seem counterintuitive,  
729 they are not contradictory since grazing cannot be equated with respiration. First, much of respiration is bacterial  
730 and therefore not reflected by the grazing rates (Robinson and Williams, 2005). Second, it has been observed that  
731 after starvation, protozoan grazers increase their organic matter production by accumulating lipids and increasing  
732 their cell size (Anderson and Menden-Deuer, 2017; Morison et al., 2020). Thus, high grazing could suggest a  
733 buildup of organic matter through secondary production, which is consistent with the higher than average  
734 microzooplankton biomass and would be reflected as large NCP. Third, microzooplankton can produce fecal pellets  
735 (Buck and Newton, 1995), removing which removes carbon from the system without respiration and thus leads  
736 to high NCP. The dominant presence, and slow growth, of large *Hemiaulus* cells within the phytoplankton  
737 community was likely a main factor promoting the higher trophic transfer efficiency from phytoplankton to  
738 microzooplankton, as is typical during winter (Marrec et al., 2021).

739 Interestingly, NCP and GOP values in summer 2018 were similar to those in August 2019 (Table 2, Fig. 75  
740 and 8) and also much higher than during subsequent summers (2020-2022), in spite of no *Hemiaulus* being present

741 in summer 2018. Additionally, the ratio of NCP/GOP in summer of 2018 was also significantly larger than in 2020-  
742 22 (Fig. 7.5 and 8). Remote sensing shows an elevated Chl-a patch (less concentrated than the patch in August 2019)  
743 in summer 2018 west of the transect that could be the driving factor behind the high NCP and GOP values (Fig.  
744 S1-S3). The summer of 2018 was dominated by small phytoplankton similar to observations in summers of 2020  
745 and 2021, although the summer of 2018 had a particularly high concentration of dinoflagellates over parts of the  
746 shelf. The summer 2018 data did not show an increase in trophic transfer efficiency due to coupled  
747 microzooplankton grazing and phytoplankton growth ~~nor did it show increased NPP.~~ The high NCP. High NCP  
748 may in summer 2018 could be due to a variety of environmental (biotic and abiotic) factors that were different from  
749 other cruises. For example, in the summer of 2018, saline waters from offshore intruded much farther inshore than  
750 during most of the other summers and these high-salinity mid-shelf waters were particularly productive (Mehta,  
751 2022). ~~Additionally, correspondence was seen between NCP and dinoflagellate biomass in summer 2018, although~~  
752 ~~this correlation was not as significant~~ as was seen with the that between *Hemiaulus* and NCP in 2019  
753 (Aldrett, 2021). Thus, this study shows that a change in community composition, such as the *Hemiaulus* bloom in  
754 August 2019, can dramatically change the productivity rates of the ecosystem ~~and yet productivity rates can also be~~  
755 ~~similarly high with even though~~ a very different phytoplankton community structure can sometimes lead to  
756 similarly high productivity.

#### 757 4.2 Aggregate vs Compositional Variability

758 The changes in community composition, productivity rates, and chlorophyll in August 2019 compared to the other  
 759 summers shed interesting light on the question of synchrony or compensation between aggregate and compositional  
 760 variability at the NES-LTER site (Micheli et al., 1999; Shoemaker et al., 2022). The resilience of an ecosystem may  
 761 be related to the compensation or synchrony between different types of variability (Lindegren et al., 2016). During  
 762 August 2019, the phytoplankton composition in the NES changed dramatically due to the bloom of the diatom  
 763 *Hemiaulus*. This change was associated with increases in Chl-a, higher productivity rates, tighter coupling between  
 764 microzooplankton grazing and phytoplankton growth, and increases in export efficiency. These latter terms are all  
 765 metrics of aggregate properties and thus this bloom event exhibited high compositional and  
 766 high aggregate variability compared to the ecosystem in July of 2020-22. Thus, during  
 767 this event, a change in metric associated with compositional variability (e.g., the change in phytoplankton community composition)  
 768 was synchronous with a change in metrics associated with aggregate variability.  
 769 However, when NCP rates are compared from the summer 2018 to summer 2019, the compositional variability composition is still  
 770 quite different (*Hemiaulus* in 2019, compared to mostly small phytoplankton in 2018) and thus there is still large compositional  
 771 variability, but the aggregate variability properties in terms of NCP is the same similar in both years—thus comparing  
 772 those two summers in a case where compositional variability changed and yet aggregate variability (at least for NCP) did  
 773 not. Why does, showing that sometimes compensation occurs in which the community composition sometimes affect NCP  
 774 dramatically (i.e., August 2019 vs July of 2020-22) and sometimes it does not (July 2018)? Perhaps NCP is affected more by the  
 775 abundance of certain species in changes but the community rather than size distribution of the community aggregate productivity does not.  
 776 This concurrent investigation of plankton community composition and production rates within a well-studied ecosystem highlights  
 777 how shifts in community size distribution can greatly affect productivity. However, it also shows that multiple factors change from year  
 778 to year, leading to different effects.

### 802 4.3 Origin of Bloom

803 The *Hemiaulus* bloom was likely more widespread than what was observed in the  
 804 NES-LTER 2019 summer cruise. For example, satellite imagery from August 11  
 805 shows a filament of warm, high Chl-a waters oriented southwest-northeast and ending in the  
 806 region where *Hemiaulus* was abundant (Fig. 10a, 11a & b); the advective continuity of the  
 807 filament with the *Hemiaulus* patch suggests the filament may have had high *Hemiaulus* as well. Direct support for a

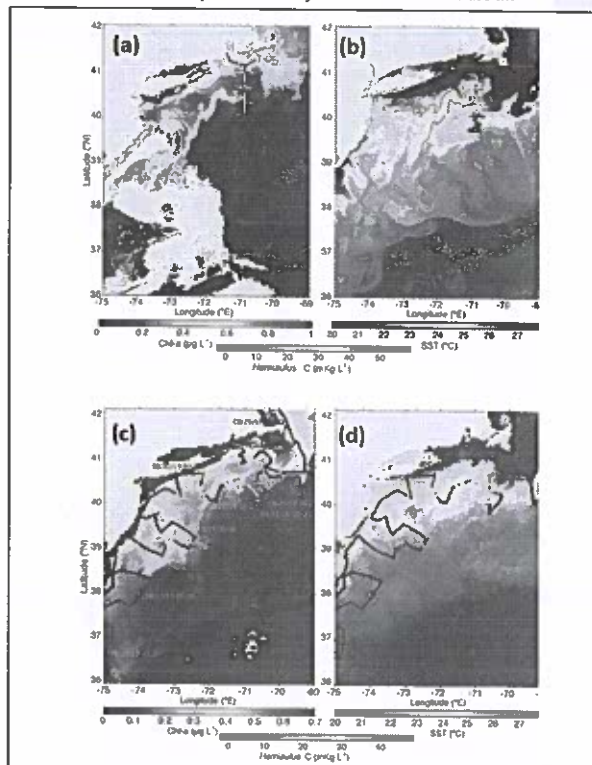


Fig. 10. Snapshots of satellite-measured (a) Chl-a and (b) SST on 11 August 2019. The 0.5 µg L<sup>-1</sup> chlorophyll contour is plotted as a solid line. *Hemiaulus* carbon from underway surface samples during the NES-LTER Aug-2019 cruise is overlaid with colored dots. The monthly composite (c) Chl-a and (d) SST for August 2019. *Hemiaulus* carbon from underway surface samples during LCOMON cruise GU1902 is overlaid with colored dots. Daily ship positions are indicated in the left panel. Animated versions of individual Chl-a and SST images are available at: [http://science.whoi.edu/users/olga/outgoing/Aug\\_2019\\_chl/NESW\\_2019-Hemiaulus/](http://science.whoi.edu/users/olga/outgoing/Aug_2019_chl/NESW_2019-Hemiaulus/)

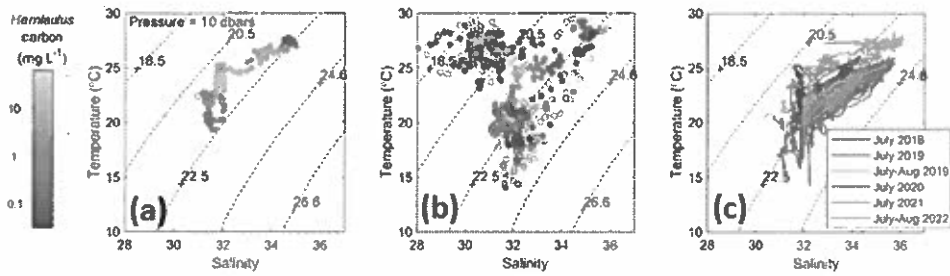


Fig 11. T-S plots, colored according to *Hemialus* carbon, suggesting that the highest *Hemialus* abundances were associated with a “sweet-spot” in T-S space that was found during (a) the 2019 summer NES-LTER cruise in August and (b) the EcoMon August 2019 cruise. Empty circles represent locations where *Hemialus* was not detected. (c) T-S plots from other years, colored according to cruise, show that a few of the other summer cruises from 2018 to 2022 have the same sweet spot in physical conditions even though they did not have detectable *Hemialus*.

812 widespread bloom comes from IFCB data collected on the NOAA EcoMon Cruise (GU1902) that occurred at a  
 813 similar time as the August 2019 NES-LTER transect cruise. The IFCB data shows that *Hemialus* was present both  
 814 farther east as well as to the southwest of where it was observed on the LTER transect cruise and that some of the  
 815 points in the high chlorophyll filament observed from satellite chlorophyll contained *Hemialus* (Fig. 40e11c).  
 816 Backward particle trajectory analysis based on HF radar-measured sea surface velocities show that the  
 817 water with high *Hemialus* biomass during the August 2019 transect cruise could have been advected from the  
 818 inner-shelf around Narragansett Bay and Georges Bank rather than from the mid-shelf further south (Fig. 84S6). In  
 819 particular, coastal upwelling probably brought the inner-shelf water into the mid-shelf transect area where it was  
 820 observed to have high *Hemialus*. The salinity of the water with the high *Hemialus* biomass is consistent with the  
 821 water having originated from the shelf. The water with high amounts of *Hemialus* carbon was associated with  
 822 salinity ranging from 31.6 to 34 psu and temperatures of 22° C to 27° C (Fig. 4412a & b). T-S plots of data from

823 other years (Fig. 4+e12c)  
 824 suggest that several other  
 825 summers also had similarly  
 826 warm, low salinity water (in  
 827 particular July of 2020 and  
 828 especially 2022) but  
 829 interestingly *Hemiaulus* were  
 830 not observed on those cruises.  
 831 Although multiple lines  
 832 of evidence suggest that the  
 833 water containing the high  
 834 biomass of *Hemiaulus* initially  
 835 originated from the inner-shelf.  
 836 *Hemiaulus* is typically found in  
 837 warm, low nutrient water –  
 838 characteristics that are not  
 839 present on the inner-shelf, where  
 840 water is instead colder and ~~often~~  
 841 ~~richer in nutrients~~ nutrient-rich.  
 842 In this case, the inner-shelf  
 843 water warmed as it was  
 844 transported offshore and thus it  
 845 reached temperatures warm  
 846 enough for *Hemiaulus* to thrive  
 847 by the time it reached the mid-  
 848 shelf (the timing of warming is  
 849 not known). But how did this  
 850 inner-shelf water acquire  
 851 *Hemiaulus* as it was transported  
 852 offshore in August 2019? One  
 853 possibility is that it was seeded  
 854 by the warmer low nutrient  
 855 surface slope and ring waters; in  
 856 particular, these slope and ring  
 857 waters were observed earlier in  
 858 the summer of 2019 to have a  
 859 small population of *Hemiaulus*  
 860 that could have served as a seed  
 861 population (Oliver et al., 2021).  
 862 However, there is no evidence  
 863 of surface transport from slope-  
 864 water to the *Hemiaulus* patch.  
 865 Another possibility is that  
 866 *Hemiaulus* were already present  
 867 in the deeper coastal water and  
 868 then thrived as the deep water  
 869 was mixed upward, warmed and  
 870 reached the higher light surface  
 871 waters. However, the vertical distributions of *Hemiaulus* (Fig. 3) do not support this hypothesis, since a deeper population was not observed. Finally, the modeled backward particle trajectories suggesting an inner-shelf origin may be inaccurate as shelf water circulation is complex, as seen by the conflicting origins of the *Hemiaulus* water to both the east and west of the transect and an inconsistency between conclusions from the particle trajectory analysis with the high Chl-a, high temperature filament observed in the Satellite imagery (Fig S6). Thus, the reason *Hemiaulus* bloomed in 2019, and not in other years, remains a topic for future research and continued speculation. Future years of the NES-LTER program may shed light on the variable effects of disturbances, such as this *Hemiaulus* bloom, as more factors that lead to high or low export in summer are determined and explored.

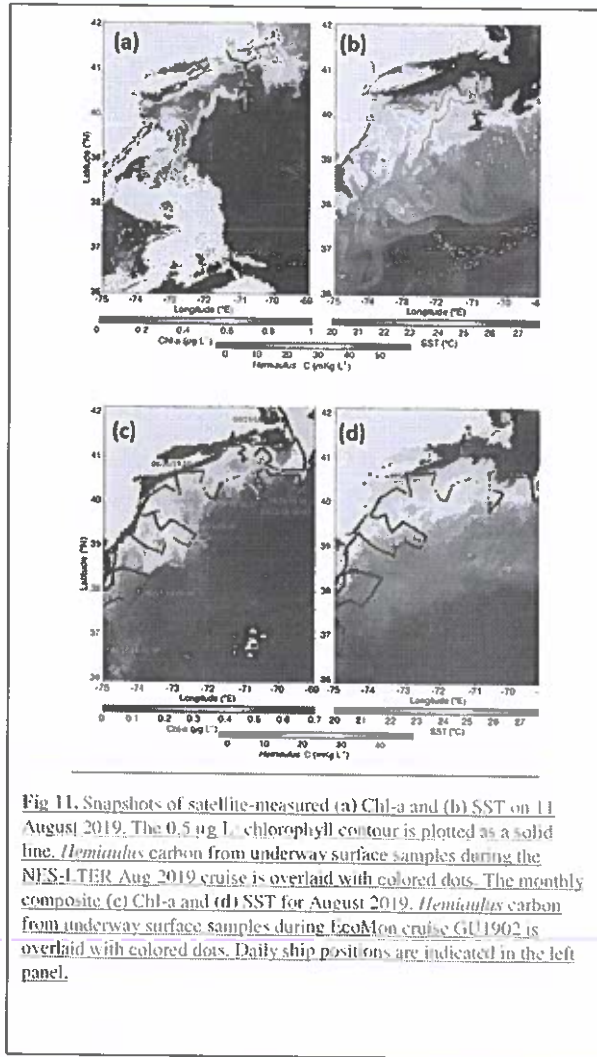


Fig 11. Snapshots of satellite-measured (a) Chl-a and (b) SST on 11 August 2019. The 0.5 µg L<sup>-1</sup> chlorophyll contour is plotted as a solid line. *Hemiaulus* carbon from underway surface samples during the NES-LTER Aug 2019 cruise is overlaid with colored dots. The monthly composite (c) Chl-a and (d) SST for August 2019. *Hemiaulus* carbon from underway surface samples during EcoMon cruise GU1902 is overlaid with colored dots. Daily ship positions are indicated in the left panel.

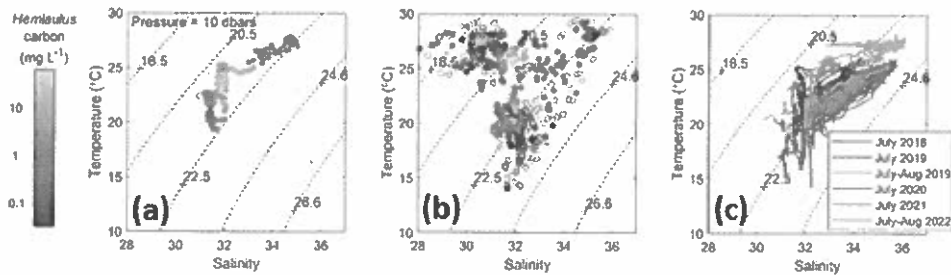


Fig 12. T-S plots, colored according to *Hemiaulus* carbon, suggesting that the highest *Hemiaulus* abundances were associated with a “sweet spot” in T-S space that was found during (a) the 2019 summer NES-LTER cruise in August and (b) the EcoMon August 2019 cruise. Empty circles represent locations where *Hemiaulus* was not detected. (c) T-S plots from other years, colored according to cruise, show that a few of the other summer cruises from 2018 to 2022 have the same sweet spot in physical conditions even though they did not have detectable *Hemiaulus*.

879

## 880 5 Conclusions

881 An unusual bloom of the diatom genus *Hemiaulus* with nitrogen-fixing symbionts in the mid-shelf region of the  
 882 Northeast U.S. shelf in August 2019 led to as observed concomitant with increases in NCP, GOP, NPP, higher  
 883 export efficiency, and higher trophic transfer efficiency from phytoplankton to microzooplankton. Very tight  
 884 coupling observed between kilometer-scale changes in NCP and the carbon biomass of *Hemiaulus* showed how a  
 885 substantial effect from the *Hemiaulus* bloom had on the aggregate variability important biogeochemical rates and  
 886 stocks of the Northeast U.S. shelf. While the source of the *Hemiaulus* on the inner-shelf remains unknown, the  
 887 bloom was associated with warmer temperatures than usually observed on the shelf which may have been an  
 888 important factor that facilitated the bloom when it was transported from the inner-shelf.

889 The *Hemiaulus* bloom, which was associated with observed at a time when there were warmer sea surface  
 890 temperatures especially in the outer-shelf region, was intriguing in that it led to unusually high productivity rates,  
 891 increases in Chl-a concentrations, and tighter food-web coupling. While the warm SST may have contributed to the  
 892 *Hemiaulus* bloom, the summer cruise of 2020 and 2022 also had showed nearly as high water temperature as  
 893 2019 in the outer-shelf and the summers of both 2020 and 2022 had anomalously similarly high water temperatures,  
 894 but as 2019 in the mid-shelf region. However, summers 2020 and 2022 had relatively low (i.e., average summer)  
 895 productivity rates and Chl-a were observed during those times. So, these summers of 2020 and 2022 had fairly  
 896 similar physical conditions to that of 2019, but no significant bloom was observed, and no high-carbon export  
 897 system was present. Thus, higher temperatures are not enough to explain higher productivity rates, a shift in  
 898 community composition is also necessary. A mixture of the right physical conditions and community composition,  
 899 like this special case of 2019, are needed for a high-carbon export system to be supported on the mid-shelf during  
 900 summer.

901 With climate change, the oceans are warming at a rapid rate, and are likely moving towards warmer more  
 902 stratified conditions (e.g., lower nitrate stock in surface waters) (Li et al., 2020) which may lead to less productivity  
 903 and thus lower export efficiencies. However, these conditions may also lead to unusual phytoplankton composition  
 904 as species shift and the work distribution shifts. The results presented here shows show that these unusual events can  
 905 lead to large locally and episodically enhanced productivity and export: despite the ecosystem commonly becoming  
 906 nitrate-limited ecosystem during the summer season, an intense phytoplankton bloom in summer occurred due to a  
 907 symbiotic diatom-diazotroph relationships relationship. These observations lead to further questions about how the  
 908 NES ecosystem is responding to the effects of climate change such as enhanced stratification. Monitoring future

909 disturbances and their effects will provide new insights into relationships, mechanisms, and patterns of composition  
910 and productivity that may be only occasionally occurring now but are likely more prevalent in the future.

## 911 **6 Data Availability**

912 All in situ data are available at the EDI data repository. In particular, the raw gas tracer data used for calculating  
913 NCP and GOP is available at  
914 <https://portal.edirepository.org/nis/mapbrowse?packageid=knb-lter-nes.6.2>. The calculated rates of NCP data is  
915 accessible at <https://portal.edirepository.org/nis/mapbrowse?packageid=knb-lter-nes.7.2>  
916 and <https://portal.edirepository.org/nis/mapbrowse?packageid=knb-lter-nes.15.2>. NPP data is available at  
917 <https://portal.edirepository.org/nis/metadataviewer?packageid=knb-lter-nes.16.4>. Grazing rate data is available at  
918 <https://portal.edirepository.org/nis/mapbrowse?packageid=knb-lter-nes.5.1>. Chlorophyll data is available at  
919 <https://portal.edirepository.org/nis/mapbrowse?packageid=knb-lter-nes.8.1>. IFCB data is available at  
920 <https://portal.edirepository.org/nis/mapbrowse?packageid=knb-lter-nes.9.1> and on the IFCB dashboard  
921 at [https://ifcb-data.whoi.edu/timeline?dataset=NESLTER\\_transect](https://ifcb-data.whoi.edu/timeline?dataset=NESLTER_transect), and <https://ifcb->  
922 [data.whoi.edu/timeline?dataset=NESLTER\\_broadscale](https://ifcb-data.whoi.edu/timeline?dataset=NESLTER_broadscale).

923  
924 The MODIS SST and chlorophyll snapshot data were produced by NASA Goddard Space Flight Center, Ocean  
925 Ecology Laboratory, Ocean Biology Processing Group, and the data are publicly available at  
926 <https://oceancolor.gsfc.nasa.gov/>. The 8-day composite data were retrieved from the public-accessible University of  
927 Delaware ERDDAP server (<https://basin.ceoe.udel.edu/erddap/index.html>) maintained by the Ocean Exploration,  
928 Remote Sensing and Biogeography Laboratory led by Dr. Matthew Oliver at University of Delaware. The HF radar-  
929 measured sea surface velocity data in July-August 2019 was obtained from the public-accessible Rutgers University  
930 Center for Ocean Observing Leadership ERDDAP server (<http://hfr.marine.rutgers.edu/erddap/griddap/>).

## 931 **Author Contribution**

932 SAC, RHRS, ZOS, and DA measured and calculated rates of productivity from gas tracers. SMD and PM measured  
933 grazing rates. TAR and DNF measured and calculated rates of net primary productivity from bottle incubations.  
934 HMS, ETC and EEP imaged and quantified phytoplankton abundances. DJM and WGZ analyzed remote sensing  
935 data. Everyone participated in study design. SAC and RHRS prepared the manuscript with contributions from all co-  
936 authors.

## 937 **Competing Interests**

938 The authors declare that they have no conflict of interest.

## 939 **Acknowledgements**

940 This work was funded by the National Science Foundation (LTER-1655686, OCE-1657489, OCE-1657803, OCE-  
941 2227425) and the Simons Foundation (561126 to HMS). S. A. Castillo Cieza was supported by the Clara Boothe  
942 Luce Fellowship program at Wellesley College. We are thankful for the scientific input, discussions and help from  
943 the entire NES-LTER science team. We are grateful to the Captain and crew of the *R/V Endeavor*. We thank Harvey  
944 Walsh, Jerome Prezioso, Audy Peoples and Tamara Holzwarth-Davis for their cooperation and enthusiasm for IFCB  
945 operations on NOAA survey cruises. We recognize the contributions of Kevin Cahill (WHOI), who ran some of the  
946 samples for triple oxygen isotope measurement, Elizabeth Lambert (Wellesley College) and Helene Alt (Wellesley  
947 College) who helped collect some of the EIMS data, and Danielle Aldrett (Wellesley College) for doing some initial  
948 analysis on connections between the IFCB and NCP data. We thank NES-LTER data manager Stace Beaulieu and  
949 Kate Morkeski (WHOI) for their help in data management. We thank URI-GSO undergraduate and graduate  
950 students and postdocs who helped collect samples and conduct experiments to obtain chl-*a* concentrations, and  
951 phytoplankton growth and microzooplankton grazing rates. We thank Sam Setta for pointing out *Hemmuthia* *Richiella*



952 in IFCB images during the 2019 summer cruise. DJM gratefully acknowledges NSF support of the SPIROPA  
953 program, and technical assistance by Olga Kosnyrev in satellite data analysis and visualization.

#### 954 References

- 955 Aldrett, D. 2021. Understanding the relationship between photosynthetic organisms and oceanic  
956 productivity in the Northeast U.S. Shelf. B.A. undergraduate thesis, *Chemistry*, Wellesley College,  
957 Wellesley, MA USA, 58 pp., 2021.
- 958 Anderson, S. R. & Menden-Deuer, S. 2017. Growth, Grazing, and Starvation Survival in Three  
959 Heterotrophic Dinoflagellate Species. *Journal of Eukaryotic Microbiology*, 64, 213-225,  
960 <https://doi.org/10.1111/jeu.12353>, 2017.
- 961 Armbrust, E. V. 2009. The life of diatoms in the world's oceans. *Nature*, 459, 185-192,  
962 [10.1038/nature08057](https://doi.org/10.1038/nature08057), 2009.
- 963 Barkan, E. & Luz, B. 2011. The relationships among the three stable isotopes of oxygen in air,  
964 seawater and marine photosynthesis. *Rapid Communications in Mass Spectrometry*, 25, 2367-2369,  
965 [10.1002/rcm.5125](https://doi.org/10.1002/rcm.5125), 2011.
- 966 Boyd, P. W., Claustre, H., Levy, M., Siegel, D. A., & Weber, T. 2019. Multi-faceted particle  
967 pumps drive carbon sequestration in the ocean. *Nature*, 568, 327-335, [10.1038/s41586-019-1098-2](https://doi.org/10.1038/s41586-019-1098-2),  
968 2019.
- 969 Brownlee, E. F., Olson, R. J., & Sosik, H. M. 2016. Microzooplankton community structure  
970 investigated with imaging flow cytometry and automated live-cell staining. *Marine Ecology Progress  
971 Series*, 550, 65-81, [10.3354/meps11687](https://doi.org/10.3354/meps11687), 2016.
- 972 Buck, K. R. & Newton, J. 1995. FECAL PELLET FLUX IN DABOB BAY DURING A DIATOM  
973 BLOOM - CONTRIBUTION OF MICROZOOPLANKTON. *Limnology and Oceanography*, 40,  
974 306-315, [10.4319/lmo.1995.40.2.0306](https://doi.org/10.4319/lmo.1995.40.2.0306), 1995.
- 975 Carpenter, E. J., Montoya, J. P., Burns, J., Mulholland, M. R., Subramaniam, A., & Capone, D. G.  
976 1999. Extensive bloom of a N-2-fixing diatom/cyanobacterial association in the tropical Atlantic  
977 Ocean. *Marine Ecology Progress Series*, 185, 273-283, [10.3354/meps185273](https://doi.org/10.3354/meps185273), 1999.
- 978 Cassar, N., Barnett, B. A., Bender, M. L., Kaiser, J., Hamme, R. C., & Tilbrook, B. 2009.  
979 Continuous High-Frequency Dissolved O-2/Ar Measurements by Equilibrator Inlet Mass  
980 Spectrometry. *Analytical Chemistry*, 81, 1855-1864, 2009.
- 981 Catlett, D., Peacock, E. E., Crockford, E. T., Futrelle, J., Batchelder, S., Stevens, B. L. F., Gast, R.,  
982 Zhang, W. C., and Sosik, H. M.: Temperature dependence of parasitoid infection and abundance of a  
983 diatom revealed by automated imaging and classification. *Proceedings of the National Academy of  
984 Science, U.S.A.*, 120, e2303356120, [doi:10.1073/pnas.2303356120](https://doi.org/10.1073/pnas.2303356120), 2023.
- 985 Cetinic, I., Poulton, N., and Slade, W. H.: Characterizing the phytoplankton soup: pump and plumbing  
986 effects on the particle assemblage in underway optical seawater systems. *Optics Express*, 24, 20703-  
987 20715, [10.1364/oe.24.020703](https://doi.org/10.1364/oe.24.020703), 2016.
- 988 Chen, B. Z. 2015. Assessing the accuracy of the "two-point" dilution technique. *Limnology and  
989 Oceanography Methods*, *Limnol. Oceanogr. Meth.*, 13, 521-526, [10.1002/lom3.10044](https://doi.org/10.1002/lom3.10044), 2015.
- 990 Chen, Z. M., Kwon, Y. O., Chen, K., Fratantoni, P., Gawarkiewicz, G., & Joyce, T. M. 2020.  
991 Long-Term SST Variability on the Northwest Atlantic Continental Shelf and Slope. *Geophysical  
992 Research Letters*, 47, [10.1029/2019gl1085455](https://doi.org/10.1029/2019gl1085455), 2020.
- 993 Coplen, T. B. 1995. Reporting of stable hydrogen, carbon, and oxygen isotopic abundances -  
994 (Technical report). *Geothermics*, 24, 708-712, 1995.
- 995 de Boyer Montegut, C., Madec, G., Fischer, A. S., Lazar, A., & Iudicone, D. 2004. Mixed layer  
996 depth over the global ocean: An examination of profile data and a profile-based climatology. *Journal  
997 of Geophysical Research*, *J. Geophys. Res.-Oceans*, 109, [10.1029/2004jc002378](https://doi.org/10.1029/2004jc002378), 2004.

Formatted: Font: Not Italic

Formatted: Indent Left: 0.06", Hanging: 0.19"

Formatted: Font: Not Italic

Formatted: Font: Not Bold

Formatted: Font: Not Italic

Formatted: Font: Not Bold

Formatted: Font: Not Italic

Formatted: Font: Not Bold

Formatted: Font: Not Italic

Formatted: Font: Not Bold

Formatted: Font: Not Italic

Formatted: Font: Not Bold

Formatted: Font: Not Italic

Formatted: Font: Not Bold

Formatted: Font: Not Italic

Formatted: Font: Not Bold

Formatted: Font: Not Italic

Formatted: Font: Not Bold

Formatted: Indent Left: 0.06", Hanging: 0.19"

Formatted: Font: Not Bold

Formatted: Font: Not Italic

Formatted: Font: Not Italic

Formatted: Font: Not Bold

Formatted: Font: Not Italic

998 Dore, J. E., Letelier, R. M., Church, M. J., Lukas, R. & Karl, D. M. 2008. Summer phytoplankton  
999 blooms in the oligotrophic North Pacific Subtropical Gyre: Historical perspective and recent  
1000 observations. *Progress in Oceanography*, 76, 2-38. [10.1016/j.pocean.2007.10.002](https://doi.org/10.1016/j.pocean.2007.10.002), 2008.

1001 Dugdale, R. C. & Goering, J. J. 1967. Uptake of new and regenerated forms of nitrogen in primary  
1002 productivity. *Limnology and Oceanography*, 12, 196-206, 1967.

1003 Emerson, S. 2014. Annual net community production and the biological carbon flux in the ocean.  
1004 *Global Biogeochemical Cycles*, 28, 14-28. [10.1002/2013gb004680](https://doi.org/10.1002/2013gb004680), 2014.

1005 Field, C. B., Behrenfeld, M. J., Randerson, J. T. & Falkowski, P. 1998. Primary production of the  
1006 biosphere: Integrating terrestrial and oceanic components. *Science*, 281, 237-240.  
1007 [10.1126/science.281.5374.237](https://doi.org/10.1126/science.281.5374.237), 1998.

1008 Finkel, Z. V., Beardall, J., Flynn, K. J., Quigg, A., Rees, T. A. V. & Raven, J. A. 2010. Phytoplankton in  
1009 a changing world: cell size and elemental stoichiometry. *Journal of Plankton Research*, 32, 119-  
1010 137.

1011 Foster, R. A. & Zehr, J. P. 2006. Characterization of diatom-cyanobacteria symbioses on the basis  
1012 of nifH, hetR and 16S rRNA sequences. *Environmental Microbiology*, *Environ. Microbiol.*, 8, 1913-  
1013 1925. [10.1111/j.1462-2920.2006.01068.x](https://doi.org/10.1111/j.1462-2920.2006.01068.x), 2006.

1014 Foster, R. A. & Zehr, J. P. 2019. Diversity, Genomics, and Distribution of Phytoplankton-  
1015 Cyanobacterium Single-Cell Symbiotic Associations. In: GOTTSMAN, S. (ed.), in: *Annual Review*  
1016 *of Microbiology*, Vol 73, edited by: Gottesman, S., Annual Review of Microbiology, 435-456,  
1017 [10.1146/annurev-micro-090817-062650](https://doi.org/10.1146/annurev-micro-090817-062650), 2019.

1018 Friedlingstein, P., Jones, M. W., O'Sullivan, M., Andrew, R. M., Bakker, D. C. E., Hauck, J., Le Quere,  
1019 C., Peters, G. P., Peters, W., Pongratz, J., Sitch, S., Canadell, J. G., Ciais, P., Jackson, R. B., Alin, S.  
1020 R., Anthoni, P., Bates, N. R., Becker, M., Bellouin, N., Bopp, L., Chau, T. T. T., Chevallier, F.,  
1021 Chini, L. P., Cronin, M., Currie, K. I., Decharme, B., Djeutchouang, L. M., Dou, X. Y., Evans, W.,  
1022 Feely, R. A., Feng, L., Gasser, T., Gilfillan, D., Gkritzalis, T., Grassi, G., Gregor, L., Gruber, N.,  
1023 Gurses, O., Harris, I., Houghton, R. A., Hurtt, G. C., Iida, Y., Ilyina, T., Luijkx, I. T., Jain, A., Jones,  
1024 S. D., Kato, E., Kennedy, D., Goldewijk, K. K., Knauer, J., Korsbakken, J. I., Kortzinger, A.,  
1025 Landschutzer, P., Lausset, S. K., Lefevre, N., Lienert, S., Liu, J. J., Marland, G., McGuire, P. C.,  
1026 Melton, J. R., Munro, D. R., Nabel, J., Nakaoka, S. I., Niwa, Y., Ono, T., Pierrot, D., Poulter, B.,  
1027 Rehder, G., Resplandy, L., Robertson, E., Rodenbeck, C., Rosan, T. M., Schwinger, J.,  
1028 Schwinghackl, C., Seferian, R., Sutton, A. J., Sweeney, C., Tanhua, T., Tans, P. P., Tian, H. Q.,  
1029 Tilbrook, B., Tubiello, F., van der Werf, G. R., Vuichard, N., Wada, C., Wanninkhof, R., Watson, A.  
1030 J., Willis, D., Wiltshire, A. J., Yuan, W. P., Yue, C., Yue, X., Zaehle, S. & Zeng, J. Y. 2022.  
1031 Global Carbon Budget 2021. *Earth System Science Data*, 14, 1917-2005. [10.5194/essd-14-1917-  
1032 2022](https://doi.org/10.5194/essd-14-1917-2022), 2022.

1033 Garcia, H. E. & Gordon, L. I. 1992. Oxygen solubility in water: better fitting equations. *Limnology*  
1034 *and Oceanography*, 37, 1307-1312, 1992.

1035 Gaysina, L. A., Saraf, A. & Singh, P. 2019. Chapter 1 - Cyanobacteria in Diverse Habitats. In:  
1036 MISHRA, in: *Cyanobacteria*, edited by: Mishra, A. K., THAWAN, D. N. & RAJ, A. N.  
1037 (eds.), *Cyanobacteria*, Academic Press, 1-28. <https://doi.org/10.1016/B978-0-12-814667-5.00001-5>,  
1038 2019.

1039 Grosse, J., Bombar, D., Hai, N. D., Lam, N. N. & Voss, M. 2010. The Mekong River plume fuels  
1040 nitrogen fixation and determines phytoplankton species distribution in the South China Sea during  
1041 low- and high-discharge season. *Limnology and Oceanography*, 55, 1668-1680.  
1042 [10.4319/lo.2010.55.4.1668](https://doi.org/10.4319/lo.2010.55.4.1668), 2010.

1043 Hama, T., Miyazaki, T., Ogawa, Y., Iwakuma, T., Takahashi, M., Otsuki, A. & Ichimura, S. 1983.  
1044 Measurement of photosynthetic production of a marine phytoplankton population using a stable <sup>13</sup>C  
1045 isotope. *Marine Biology*, 73, 31-36. [10.1007/BF00396282](https://doi.org/10.1007/BF00396282), 1983.

1046 Hamme, R. C. & Emerson, S. 2004. The solubility of neon, nitrogen and argon in distilled water  
1047 and seawater. *Deep Sea Research I*, 51, 1517-1528, 2004.

Formatted: Font: Not Italic

Formatted: Font: Not Bold

Formatted: Font: Not Italic

Formatted: Font: Not Bold

Formatted: Font: Not Italic

Formatted: Font: Not Bold

Formatted: Font: Not Italic

Formatted: Font: Not Bold

Formatted: Indent Left: 0.06", Hanging: 0.19"

Formatted: Font: Not Bold

Formatted: Font: Not Italic

Formatted: Font: Not Italic

Formatted: Font: Not Italic

Formatted: Font: Not Bold

Formatted: Font: Not Italic

Formatted: Font: Not Bold

Formatted: Font: Not Italic

Formatted: Font: Not Bold

Formatted: Font: Not Italic

Formatted: Font: Not Bold

Formatted: Font: Not Italic

Formatted: Font: Not Bold

Formatted: Font: Not Italic

Formatted: Font: Not Bold

Formatted: Font: Not Italic

Formatted: Font: Not Bold

1048 Hendricks, M. B., Bender, M. L. & Barnett, B. A. 2004. Net and gross O<sub>2</sub> production in the  
 1049 Southern Ocean from measurements of biological O<sub>2</sub> saturation and its triple isotope composition.  
 1050 *Deep-Sea Research Res. Part I-Oceanographic Research Papers*, *Oceanogr. Res. Pap.*, 51, 1541-1561,  
 1051 2004.

1052 Jakobsen, H. H. and Markager, S. Carbon to chlorophyll ratio for phytoplankton in temperate coastal  
 1053 waters: Seasonal patterns and relationship to nutrients. *Limnology and Oceanography*, 61, 1853-  
 1054 1868, doi:10.1002/lno.10338, 2016.

1055 Jin, X., Gruber, N., Dunne, J. P., Sarmiento, J. L. & Armstrong, R. A. 2006. Diagnosing the  
 1056 contribution of phytoplankton functional groups to the production and export of particulate organic  
 1057 carbon, CaCO<sub>3</sub>, and opal from global nutrient and alkalinity distributions. *Global Biogeochemical*  
 1058 *Cycles*, 20, 10.1029/2005gb002532, 2006.

1059 Juranek, L. W., Hamme, R. C., Kaiser, J., Wanninkhof, R. & Quay, P. D. 2010. Evidence of O<sub>2</sub>  
 1060 consumption in underway seawater lines: Implications for air-sea O<sub>2</sub> and CO<sub>2</sub> fluxes.  
 1061 *Geophysical Research Letters*, 37, doi:10.1029/2009GL040423.

1062 Juranek, L. W. & Quay, P. D. 2005. Juranek, L. W. and Quay, P. D.: In vitro and in situ gross primary  
 1063 and net community production in the North Pacific Subtropical Gyre using labeled and natural  
 1064 abundance isotopes of dissolved O<sub>2</sub>. *Global Biogeochemical Cycles*, 19,  
 1065 doi:10.1029/2004GB002384, 2005.

1066 Juranek, L. W. & Quay, P. D. 2013. Using Triple Isotopes of Dissolved Oxygen to Evaluate Global  
 1067 Marine Productivity. In: CARLSON, C. A. & GIOVANNONI, S. J. (eds.), in *Annual Review of*  
 1068 *Marine Science*, Vol 5. Palo Alto, edited by: Carlson, C. A., and Giovannoni, S. J., *Annual Review*  
 1069 *of Marine Science*, Annual Reviews, Palo Alto, 503-524, 10.1146/annurev-marine-121211-172430,  
 1070 2013.

1071 Juranek, L. W., Hamme, R. C., Kaiser, J., Wanninkhof, R., and Quay, P. D.: Evidence of O<sub>2</sub>  
 1072 consumption in underway seawater lines: Implications for air-sea O<sub>2</sub> and CO<sub>2</sub> fluxes. *Geophysical*  
 1073 *Research Letters*, 37, doi:10.1029/2009GL040423, 2010.

1074 Kalnay, E., Kanamitsu, M., Kistler, R., Collins, W., Deaven, D., Gandin, L., Iredell, M., Saha, S., White,  
 1075 G., Woollen, J., Zhu, Y., Chelliah, M., Ebisuzaki, W., Higgins, W., Janowiak, J., Mo, K. C.,  
 1076 Ropelewski, C., Wang, J., Leetmaa, A., Reynolds, R., Jenne, R. & Joseph, D. 1996. The  
 1077 NCEP/NCAR 40-year reanalysis project. *Bulletin of the American Meteorological Society*, 77, 437-  
 1078 471, 10.1175/1520-0477(1996)077<0437:TNYRP>2.0.CO;2, 1996.

1079 Kara, A. B., Rochford, P. A. & Hurlburt, H. E. 2000. An optimal definition for ocean mixed layer  
 1080 depth. *Journal of Geophysical Research*, *J. Geophys. Res. Oceans*, 105, 16803-16821,  
 1081 10.1029/2000jc900072, 2000.

1082 Karl, D. M., Church, M. J., Dore, J. E., Letelier, R. M. & Mahaffey, C. 2012. Predictable and  
 1083 efficient carbon sequestration in the North Pacific Ocean supported by symbiotic nitrogen fixation.  
 1084 *Proceedings of the National Academy of Sciences of the United States of America*, 109, 1842-1849,  
 1085 10.1073/pnas.1120312109, 2012.

1086 Karmalkar, A. V. & Horton, R. M. 2021. Drivers of exceptional coastal warming in the northeastern  
 1087 United States. *Nature Climate Change*, 11, 854-861, 10.1038/s41558-021-01159-7, 2021.

1088 Kemp, A. E. S. & Villareal, T. A. 2013. High diatom production and export in stratified waters - A  
 1089 potential negative feedback to global warming. *Progress in Oceanography*, 119, 4-23,  
 1090 10.1016/j.pocean.2013.06.004, 2013.

1091 Kemp, A. E. S. & Villareal, T. A. 2018. The case of the diatoms and the muddled mandalas: Time  
 1092 to recognize diatom adaptations to stratified waters. *Progress in Oceanography*, 167, 138-149,  
 1093 10.1016/j.pocean.2018.08.002, 2018.

1094 Kistler, R., Kalnay, E., Collins, W., Saha, S., White, G., Woollen, J., Chelliah, M., Ebisuzaki, W.,  
 1095 Kanamitsu, M., Kousky, V., van den Dool, H., Jenne, R. & Fiorino, M. 2001. The NCEP-  
 1096 NCAR 50-year reanalysis: Monthly means CD-ROM and documentation. *Bulletin of the American*  
 1097 *Meteorological Society*, 82, 247-267, 2001.

Formatted: Font: Not Italic

Formatted: Font: Not Italic

Formatted: Font: Not Bold

Formatted: Indent Left: 0.06", Hanging: 0.19"

Formatted: Font: Not Italic

Formatted: Indent Left: 0.06", Hanging: 0.19"

Formatted: Font: Not Italic

Formatted: Font: Not Bold

Formatted: Font: Not Italic

Formatted: Indent Left: 0.06", Hanging: 0.19"

Formatted: Font: Not Italic

Formatted: Font: Not Bold

Formatted: Font: Not Italic

Formatted: Font: Not Bold

Formatted: Font: Not Italic

Formatted: Font: Not Bold

Formatted: Font: Not Italic

Formatted: Font: Not Bold

Formatted: Font: Not Italic

Formatted: Font: Not Bold

Formatted: Font: Not Italic

Formatted: Font: Not Bold

Formatted: Font: Not Italic

Formatted: Font: Not Bold

1098 Landry, M. R. and Calbet, A.: Microzooplankton production in the oceans, *ICES J. Mar. Sci.*, 61, 501-  
1099 507, [10.1016/j.icesjms.2004.03.011](https://doi.org/10.1016/j.icesjms.2004.03.011), 2004.

1100 Landry, M. R., Brown, S. L., Neveux, J., Dupouy, C. J. B., Christensen, S., and Bidigare, R. R.:  
1101 Phytoplankton growth and microzooplankton grazing in high-nutrient, low-chlorophyll waters of the  
1102 equatorial Pacific: Community and taxon-specific rate assessments from pigment and flow cytometric  
1103 analyses, *JGR Oceans*, 108, <https://doi.org/10.1029/2000JC000744>, 2003.

1104 Landry, M. R., Brown, S. L., Rii, Y. M., Selph, K. E., Bidigare, R. R., Yang, E. J., and Simmons, M. P.:  
1105 Depth-stratified phytoplankton dynamics in Cyclone Opal, a subtropical mesoscale eddy, *Deep-Sea  
1106 Research Part II-Topical Studies in Oceanography*, 55, 1348-1359, [10.1016/j.dsr2.2008.02.001](https://doi.org/10.1016/j.dsr2.2008.02.001), 2008.

1107  
1108 Landry, M. R. & Calbet, A. 2004. Microzooplankton production in the oceans. *ICES Journal of Marine  
1109 Science*, 61, 501-507.

1110 Lange, M. and van Sebille, E.: 2017, Parcels v0.9: prototyping a Lagrangian ocean analysis  
1111 framework for the petascale age, *Geosci. Model Dev.*, 10, 4175-4186, [10.5194/gmd-10-4175-2017](https://doi.org/10.5194/gmd-10-4175-2017),  
1112 2017.

1113 Li, G. C., Cheng, L. J., Zhu, J., Trenberth, K. E., Mann, M. E., and Abraham, J. P.: 2020, Increasing  
1114 ocean stratification over the past half-century, *Nature Climate Change*, 10, 1116-1126, [10.1038/s41558-020-00918-2](https://doi.org/10.1038/s41558-020-00918-2), 2020.

1115  
1116 Li, Y., Fratantoni, P. S., Chen, C. S., Hare, J. A., Sun, Y. F., Beardsley, R. C., and Ji, R. B.: 2015,   
1117 Spatio-temporal patterns of stratification on the Northwest Atlantic shelf, *Progress in Oceanography*,  
1118 134, 123-137, [10.1016/j.pocean.2015.01.003](https://doi.org/10.1016/j.pocean.2015.01.003), 2015.

1119 Lindgren, M., Checkley, D. M., Ohman, M. D., Koslow, J. A., and Goericke, R.: 2016, Resilience  
1120 and stability of a pelagic marine ecosystem, *Proceedings of the Royal Society B-Biological Sciences*,  
1121 283, [10.1098/rspb.2015.1931](https://doi.org/10.1098/rspb.2015.1931), 2016.

1122 Lomas, M. W., Moran, S. B., Casey, J. R., Bell, D. W., Tiahlo, M., Whitefield, J., Kelly, R. P., Mathis, J.  
1123 T., and Cokelet, E. D.: 2012, Spatial and seasonal variability of primary production on the Eastern  
1124 Bering Sea shelf, *Deep-Sea Research Part II-Topical Studies in Oceanography*, 65-70, 126-140,  
1125 [10.1016/j.dsr2.2012.02.010](https://doi.org/10.1016/j.dsr2.2012.02.010), 2012.

1126 Malviya, S., Scalco, E., Audic, S., Vincenta, F., Veluchamy, A., Poulain, J., Wincker, P., Iudicone, D.,  
1127 de Vargas, C., Bittner, L., Zingone, A., and Bowler, C.: 2016, Insights into global diatom  
1128 distribution and diversity in the world's oceans, *Proceedings of the National Academy of Sciences of  
1129 the United States of America*, 113, E1516-E1525, [10.1073/pnas.1509523113](https://doi.org/10.1073/pnas.1509523113), 2016.

1130 Manning, C., Stanley, R. H. R., and Lott III, D. E.: 2016, Continuous Measurements of Dissolved  
1131 Ne, Ar, Kr, and Xe Ratios with a Field-deployable Gas Equilibration Mass Spectrometer, *Analytical  
1132 Chemistry*, 88, 3040-3048, [doi: 10.1021/acs.analchem.5b03102](https://doi.org/10.1021/acs.analchem.5b03102), 2016.

1133 Manning, C. C., Howard, E. M., Nicholson, D. P., Ji, B. Y., Sandwith, Z. O., and Stanley, R. H. R.:  
1134 2017a, Revising estimates of aquatic gross oxygen production by the triple oxygen isotope method  
1135 to incorporate the local isotopic composition of water, *Geophysical Research Letters*, 44,  
1136 [10.1002/2017GL074375](https://doi.org/10.1002/2017GL074375), 2017a.

1137 Manning, C. C., Stanley, R. H. R., Nicholson, D. P., Smith, J. M., Pennington, J. T., Fewings, M. R.,  
1138 Squibb, M. E., and Chavez, F. P.: 2017b, Impact of recently upwelled water on productivity  
1139 investigated using in situ and incubation-based methods in Monterey Bay, *Journal of Geophysical  
1140 Research*, J. Geophys. Res.-Oceans, 122, 1901-1926, [10.1002/2016JC012306](https://doi.org/10.1002/2016JC012306), 2017b.

1141 Margalef, R.: Life-forms of phytoplankton as survival alternatives in an unstable environment,  
1142 *Oceanologica Acta*, 1, 493-509, 1978.

1143 Marrec, P., McNair, H., Franze, G., Morison, F., Strock, J. P., and Menden-Deuer, S.: 2021, Seasonal  
1144 variability in planktonic food web structure and function of the Northeast US Shelf, *Limnology and  
1145 Oceanography*, 66, 1440-1458, [10.1002/lno.11696](https://doi.org/10.1002/lno.11696), 2021.

1146 Mehta, A.: 2022, Spatial and Temporal Heterogeneity in Net Community Production in the Crossshelf  
1147 Direction of the Atlantic Northeastern Shelf. B.A., undergraduate thesis, Chemistry, Wellesley  
1148 College, Wellesley, MA USA, 86 pp., 2022.

Formatted: Indent Left: 0.06", Hanging: 0.19"

Formatted: Font: Not Italic

Formatted: Font: Not Bold

Formatted: Indent Left: 0.06", Hanging: 0.19"

Formatted: Font: Not Italic

Formatted: Font: Not Bold

Formatted: Font: Not Italic

Formatted: Font: Not Bold

Formatted: Font: Not Italic

Formatted: Font: Not Bold

Formatted: Font: Not Italic

Formatted: Font: Not Italic

Formatted: Font: Not Bold

Formatted: Font: Not Italic

Formatted: Font: Not Bold

Formatted: Font: Not Italic

Formatted: Font: Not Bold

Formatted: Font: Not Italic

Formatted: Font: Not Italic

Formatted: Font: Not Bold

Formatted: Indent Left: 0.06", Hanging: 0.19"

Formatted: Font: Not Italic

Formatted: Font: Not Bold

Formatted: Font: Not Italic

1149 Menden-Deuer, S. & Lessard, E. (2000). Menden-Deuer S, Lessard EJ. Carbon to volume  
1150 relationships for dinoflagellates, diatoms, and other protist plankton. *Limnol Oceanogr* 45: 569-579,  
1151 *Limnology and oceanography*, 45, 569-579, [10.4319/lom.2000.45.3.0569](https://doi.org/10.4319/lom.2000.45.3.0569), 2000.

1152 Micheli, F., Cottingham, K. L., Bascompte, J., Bjornstad, O. N., Eckert, G. L., Fischer, J. M., Keitt, T.  
1153 H., Kendall, B. E., Klug, J. L. & Rusak, J. A. (1999). The dual nature of community variability.  
1154 *Oikos*, 85, 161-169, [10.2307/3546802](https://doi.org/10.2307/3546802), 1999.

1155 Millero, F. J. & Poisson, A. (1984). International One-Atmosphere Equation of State of Seawater.  
1156 *Deep-Sea Research Part a-Oceanographic Research Papers*, 28, 625-629, 1981.

1157 Moberg, E. A. & Sosik, H. M. (2012). Distance maps to estimate cell volume from two-dimensional  
1158 plankton images. *Limnology and Oceanography Methods*, *Limnol. Oceanogr. Meth.*, 10, 278-288,  
1159 [10.4319/lom.2012.10.278](https://doi.org/10.4319/lom.2012.10.278), 2012.

1160 Morison, F., Franzè, G., Harvey, E. & Menden-Deuer, S. (2020). Light fluctuations are key in  
1161 modulating plankton trophic dynamics and their impact on primary production. *Limnology and*  
1162 *Oceanography Letters*, 5, 346-353, <https://doi.org/10.1002/lol2.10156>, 2020.

1163 Mouw, C. B. & Yoder, J. A. (2005). Primary production calculations in the Mid-Atlantic Bight,  
1164 including effects of phytoplankton community size structure. *Limnology and Oceanography*, 50,  
1165 1232-1243, 2005.

1166 O'Reilly, J. E. & Zetlin, C. (1998). Seasonal, horizontal and vertical distribution of phytoplankton  
1167 chlorophyll a in the Northeast U.S. Continental Shelf Ecosystem. *NOAA Tech. Rep.*, 1998.

1168 Oliver, H., Zhang, W. F., Smith, W. O., Alatalo, P., Chappell, P. D., Hirzel, A. J., Selden, C. R., Sosik, H.  
1169 M., Stanley, R. H. R., Zhu, Y. F. & McGillicuddy, D. J. (2021). Diatom Hotspots Driven by  
1170 Western Boundary Current Instability. *Geophysical Research Letters*, 48.

1171 Oliver, H., Zhang, W. G., Archibald, K. M., Hirzel, A. J., Smith, W. O., Sosik, H. M., Stanley, R. H. R.  
1172 & McGillicuddy, D. J. (2022). Ephemeral Surface Chlorophyll Enhancement at the New  
1173 England Shelf Break Driven by Ekman Restratification. *Journal of Geophysical Research*, *J.*  
1174 *Geophys. Res.-Oceans*, 127, [10.1029/2021jc017715](https://doi.org/10.1029/2021jc017715), 2022.

1175 Oliver, H., Zhang, W. F., Smith, W. O., Alatalo, P., Chappell, P. D., Hirzel, A. J., Selden, C. R., Sosik,  
1176 H. M., Stanley, R. H. R., Zhu, Y. F., & McGillicuddy, D. J.: Diatom Hotspots Driven by Western  
1177 Boundary Current Instability. *Geophysical Research Letters*, 48, [10.1029/2020gl091943](https://doi.org/10.1029/2020gl091943), 2021.

1178 Olson, R. J. & Sosik, H. M. (2007). A submersible imaging-in-flow instrument to analyze nano-and  
1179 microplankton: Imaging FlowCytobot. *Limnology and Oceanography Methods*, *Limnol. Oceanogr.*  
1180 *Meth.*, 5, 195-203, [10.4319/lom.2007.5.195](https://doi.org/10.4319/lom.2007.5.195), 2007.

1181 Palevsky, H. I., Quay, P. D., Lockwood, D. E. & Nicholson, D. P. (2016). The annual cycle of gross  
1182 primary production, net community production, and export efficiency across the North Pacific  
1183 Ocean. *Global Biogeochem. Cycles*, 30, 361-380, [10.1002/2015GB005318](https://doi.org/10.1002/2015GB005318), 2016.

1184 Parsons, T. R., Maita, Y. & Lalli, C. M. (1984). A Manual of Chemical & Biological Methods for  
1185 Seawater Analysis, Pergamon, <https://doi.org/10.1016/C2009-0-07774-5>, 1984.

1186 Prokopenko, M. G., Pauluis, O. M., Granger, J. & Yeung, L. Y. (2011). Exact evaluation of gross  
1187 photosynthetic production from the oxygen triple-isotope composition of O(2): Implications for the  
1188 net-to-gross primary production ratios. *Geophysical Research Letters*, 38,  
1189 [L1460310.1029/2011gl047652](https://doi.org/10.1029/2011gl047652), 2011.

1190 Puigcorbe, V., Benitez-Nelson, C. R., Masque, P., Verdeny, E., White, A. E., Popp, B. N., Prahl, F. G.  
1191 & Lam, P. J. (2015). Small phytoplankton drive high summertime carbon and nutrient export in  
1192 the Gulf of California and Eastern Tropical North Pacific. *Global Biogeochemical Cycles*, 29, 1309-  
1193 1332, [10.1002/2015gb005134](https://doi.org/10.1002/2015gb005134), 2015.

1194 Pyle, A. E., Johnson, A. M. & Villareal, T. A. (2020). Isolation, growth, and nitrogen fixation rates  
1195 of the *Hemiaulus-Richelia* (diatom-cyanobacterium) symbiosis in culture. *PeerJ*, 8,  
1196 [10.7717/peerj.10115](https://doi.org/10.7717/peerj.10115), 2020.

1197 Reuer, M. K., Barnett, B. A., Bender, M. L., Falkowski, P. G. & Hendricks, M. B. (2007). New  
1198 estimates of Southern Ocean biological production rates from O-2/Ar ratios and the triple isotope

Formatted: Font Not Italic

Formatted: Font Not Bold

Formatted: Font Not Italic

Formatted: Font Not Bold

Formatted: Font Not Italic

Formatted: Font Not Bold

Formatted: Font Not Bold

Formatted: Font Not Italic

Formatted: Font Not Bold

Formatted: Font Not Italic

Formatted: Font Not Bold

Formatted: Indent Left: 0.06", Hanging: 0.19"

Formatted: Font Not Italic

Formatted: Indent Left: 0.06", Hanging: 0.19"

Formatted: Font Not Bold

Formatted: Font Not Italic

Formatted: Font Not Bold

Formatted: Font Not Italic

Formatted: Font Not Italic

Formatted: Font Not Italic

Formatted: Font Not Italic

Formatted: Font Not Bold

Formatted: Font Not Italic

1199 composition of O-2, *Deep-Sea Research Res. Part I-Oceanographic Research Papers-Oceanogr. Res.*  
1200 *Pap.*, 54, 951-974, 2007.

1201 Robinson, C. & Williams, P. J. I. B. 2005. 147 Respiration and its measurement in surface marine  
1202 waters. *Respiration in Aquatic Ecosystems*. Oxford University Press,  
1203 10.1093/acprof:oso/9780198527084.003.0009, 2005.

1204 Russakovsky, O., Deng, J., Su, H., Krause, J., Satheesh, S., Ma, S., Huang, Z. H., Karpathy, A., Khosla,  
1205 A., Bernstein, M., Berg, A. C. & Fei-Fei, L. 2015. ImageNet Large Scale Visual Recognition  
1206 Challenge. *International Journal of Computer Vision*, 115, 211-252. 10.1007/s11263-015-0816-y,  
1207 2015.

1208 Schmoker, C., Hernandez-Leon, S. & Calbet, A. 2013. Microzooplankton grazing in the oceans:  
1209 impacts, data variability, knowledge gaps and future directions. *Journal of Plankton Research*, 35,  
1210 691-706. 10.1093/plankt/fbt023, 2013.

1211 Shearman, R. K. & Lentz, S. J. 2010. Long-Term Sea Surface Temperature Variability along the US  
1212 East Coast. *Journal of Physical Oceanography*, J. Phys. Oceanogr., 40, 1004-1017,  
1213 10.1175/2009jpo4300.1, 2010.

1214 Shoemaker, L. G., Hallett, L. M., Zhao, L., Reuman, D. C., Wang, S. P., Cottingham, K. L., Hobbs, R.  
1215 J., Castorani, M. C. N., Downing, A. L., Dudney, J. C., Fey, S. B., Gherardi, L. A., Lany, N.,  
1216 Portales-Reyes, C., Rypel, A. L., Sheppard, L. W., Walter, J. A. & Suding, K. N. 2022. The  
1217 long and the short of it: Mechanisms of synchronous and compensatory dynamics across temporal  
1218 scales. *Ecology*, 103, 10.1002/ecy.3650, 2022.

1219 Spitzer, S. 2015. An Analysis of Diatom Growth Rate and the Implications for the Biodiesel Industry.  
1220 *Occum's Razor*, 5, 2015.

1221 Stanley, R. H. R., Jenkins, W. J., Doney, S. C. & Lott III, D. E. 2009. Noble Gas Constraints on Air-Sea  
1222 Gas Exchange and Bubble Fluxes. *Journal of Geophysical Research - Oceans*, 114,  
1223 doi:10.1029/2009JC005396.

1224 Stanley, R. H. R., Kirkpatrick, J. B., Barnett, B., Cassar, N. & Bender, M. L. 2010. Net community  
1225 production and gross production rates in the Western Equatorial Pacific. *Global Biogeochemical*  
1226 *Cycles*, 24, GB4001, doi:10.1029/2009GB003651.

1227 Stanley, R. H. R., Sandwith, Z. O. & Williams, W. J. 2015. Rates of summertime biological  
1228 productivity in the Beaufort Gyre: A comparison between the low and record-low ice conditions of  
1229 August 2011 and 2012. *Journal of Marine Systems*, 147, 29-44, 2015.

1230 Stanley, R. H. R., Jenkins, W. J., Doney, S. C., and Lott III, D. E. Noble Gas Constraints on Air-Sea  
1231 Gas Exchange and Bubble Fluxes. *Journal of Geophysical Research - Oceans*, 114,  
1232 doi:10.1029/2009JC005396, 2009.

1233 Stanley, R. H. R., Kirkpatrick, J. B., Barnett, B., Cassar, N., and Bender, M. L. Net community  
1234 production and gross production rates in the Western Equatorial Pacific. *Global Biogeochemical*  
1235 *Cycles*, 24, GB4001, doi:10.1029/2009GB003651, 2010.

1236 Subramaniam, A., Yager, P. L., Carpenter, E. J., Mahaffey, C., Bjorkman, K., Cooley, S., Kustka, A. B.,  
1237 Montoya, J. P., Sanudo-Wilhelmy, S. A., Shipe, R. & Capone, D. G. 2008. Amazon River  
1238 enhances diazotrophy and carbon sequestration in the tropical North Atlantic Ocean. *Proceedings of*  
1239 *the National Academy of Sciences of the United States of America*, 105, 10460-10465,  
1240 10.1073/pnas.0710279105, 2008.

1241 Szegedy, C., Vanhoucke, V., Ioffe, S., Shlens, J. & Wojna, Z. Rethinking the Inception  
1242 Architecture for Computer Vision. 2016 IEEE Conference on Computer Vision and Pattern  
1243 Recognition (CVPR), 27-30 June 2016-2016, 2818-2826. 10.1109/CVPR.2016.308.

1244 Tang, W. Y., Cerdan-García, E., Berthelot, H., Polyviou, D., Wang, S. V., Baylay, A., Whitby, H.,  
1245 Planquette, H., Mowlem, M., Robidart, J. & Cassar, N. 2020. New insights into the  
1246 distributions of nitrogen fixation and diazotrophs revealed by high-resolution sensing and sampling  
1247 methods. *Isme Journal*, 14, 2514-2526. 10.1038/s41396-020-0703-6, 2020.

Formatted: Font: Not Italic

Formatted: Font: Not Italic

Formatted: Font: Not Bold

Formatted: Font: Not Italic

Formatted: Font: Not Bold

Formatted: Font: Not Italic

Formatted: Font: Not Bold

Formatted: Font: Not Bold

Formatted: Font: Not Italic

Formatted: Font: Not Italic

Formatted: Indent Left: 0.06", Hanging: 0.19"

Formatted: Font: Not Italic

Formatted: Font: Not Bold

Formatted: Indent Left: 0.06", Hanging: 0.19"

Formatted: Font: Not Italic

Formatted: Font: Not Bold

Formatted: Font: Not Italic

Formatted: Font: Not Bold

1248 Teeter, L., Hamme, R. C., Ianson, D. &, and Bianucci, L. 2018. Accurate estimation of net community  
 1249 production from O<sub>2</sub>/Ar measurements. *Global Biogeochem. Cycles*, 32, 10.1029/2017GB005874,  
 1250 2018.

1251 Townsend, D. W., Thomas, A. C., Mayer, L. M., Thomas, A. J. &, and Quinlan, J. A. 2006.  
 1252 Oceanography of the Northwest Atlantic continental shelf. In ROBINSON, in: *The Sea*, edited by:  
 1253 Robinson, A. R. & BRINK, and Brink, K. H. (eds.) *The Sea*. Harvard University Press, 119-167,  
 1254 2006.

1255 Twining, B. S., Nodder, S. D., King, A. L., Hutchins, D. A., LeClerc, G. R., DeBruyn, J. M., Maas, E.  
 1256 W., Vogt, S., Wilhelm, S. W. &, and Boyd, P. W. 2014. Differential remineralization of major and  
 1257 trace elements in sinking diatoms. *Limnology and Oceanography*, 59, 689-704.  
 1258 10.4319/lno.2014.59.3.0689, 2014.

1259 Villareal, T. A.: Laboratory culture and preliminary characterization of the nitrogen-fixing Rhizosolenia-  
 1260 Richelia symbiosis. *Marine Ecology*, 11, 117-132, 1990.

1261 Villareal, T. A., Adornato, L., Wilson, C. &, and Schoenbaechler, C. A. 2011. Summer blooms of  
 1262 diatom-diazotroph assemblages and surface chlorophyll in the North Pacific gyre: A disconnect.  
 1263 *Journal of Geophysical Research*. J. Geophys. Res.: Oceans, 116, 10.1029/2010jc006268, 2011.

1264 Wang, S., Tang, W. Y., Delage, E., Gifford, S., Whitby, H., Gonzalez, A. G., Eveillard, D., Planquette,  
 1265 H. &, and Cassar, N. 2021. Investigating the microbial ecology of coastal hotspots of marine  
 1266 nitrogen fixation in the western North Atlantic. *Scientific Reports*, 11, 10.1038/s41598-021-84969-1,  
 1267 2021.

1268 Yoder, J. A., Schollaert, S. E. &, and O'Reilly, J. E. 2002. Climatological phytoplankton chlorophyll  
 1269 and sea surface temperature patterns in continental shelf and slope waters off the northeast US coast.  
 1270 *Limnology and Oceanography*, 47, 672-682, 2002.

1271 Zhang, W. F., Alatalo, P., Crockford, T., Hirzel, A. J., Meyer, M. G., Oliver, H., Peacock, E., Petitpas,  
 1272 C. M., Sandwith, Z., Smith, W. O., Sosik, H. M., Stanley, R. H. R., Stevens, B. L. F., Turner, J. T. &,  
 1273 and McGillicuddy, D. J. 2023. Cross-shelf exchange associated with a shelf-water streamer at the  
 1274 Mid-Atlantic Bight shelf edge. *Progress in Oceanography*, 210, 10.1016/j.pocan.2022.102931,  
 1275 2023.

Formatted: Font: Not Italic

Formatted: Font: Not Italic

Formatted: Font: Not Bold

Formatted: Indent: Left: 0.06", Hanging: 0.19"

Formatted: Font: Not Italic

Formatted: Font: Not Italic

Formatted: Font: Not Italic

Formatted: Font: Not Bold

Formatted: Font: Not Italic

**Page 18: [1] Deleted Cells** Rachel Stanley 12/21/2023 1:21:00 PM

Deleted Cells

**Page 18: [2] Deleted Cells** Rachel Stanley 12/21/2023 1:21:00 PM

Deleted Cells

**Page 18: [3] Formatted** Rachel Stanley 12/21/2023 1:21:00 PM

Font: 8 pt, Font color: Black

**Page 18: [4] Formatted** Rachel Stanley 12/21/2023 1:21:00 PM

Left, Indent: Left: -0.08"

**Page 18: [5] Formatted** Rachel Stanley 12/21/2023 1:21:00 PM

Font: 7 pt, Font color: Black

**Page 18: [5] Formatted** Rachel Stanley 12/21/2023 1:21:00 PM

Font: 7 pt, Font color: Black

**Page 18: [6] Formatted** Rachel Stanley 12/21/2023 1:21:00 PM

Font: 8 pt, Bold, Font color: Black

**Page 18: [6] Formatted** Rachel Stanley 12/21/2023 1:21:00 PM

Font: 8 pt, Bold, Font color: Black

**Page 18: [7] Formatted** Rachel Stanley 12/21/2023 1:21:00 PM

Font: 8 pt, Font color: Black

**Page 18: [8] Formatted** Rachel Stanley 12/21/2023 1:21:00 PM

Font: 8 pt, Font color: Black

**Page 18: [9] Formatted** Rachel Stanley 12/21/2023 1:21:00 PM

Font: 8 pt, Bold, Font color: Black

**Page 18: [10] Formatted** Rachel Stanley 12/21/2023 1:21:00 PM

Font: 8 pt, Font color: Black

**Page 18: [11] Formatted** Rachel Stanley 12/21/2023 1:21:00 PM

Font: 8 pt, Font color: Black

**Page 18: [12] Formatted** Rachel Stanley 12/21/2023 1:21:00 PM

Font: 8 pt, Bold, Font color: Black